Eidgenössische Technische Hochschule Zürich
Swiss Federal Institute of Technology Zurich

Institute for Atmospheric and Climate Science

Master Thesis

# Diabatic processes associated with an extratropical dry intrusion reaching into the western North Atlantic trade wind region

Earth Sciences, ETH Zurich
Institute for Atmospheric and Climate Science

Dr. Franziska Aemisegger, Institute for Atmospheric and Climate Science, ETH Zurich
Leonie Villiger, Institute for Atmospheric and Climate Science, ETH Zurich
Dr. Maxi Boettcher, Institute for Atmospheric and Climate Science, ETH Zurich

Submitted by: Sara Müller
15-936-503
Zurich, 16 March 2021

**Abstract**

Intrusions of dry upper-level extratropical air into the tropics play an important role in shaping the synoptic time-scale variability of the low-level cloud cover over the tropical oceans. In this study, we present a detailed Lagrangian analysis of an extratropical dry intrusion in the western North Atlantic, which occurred in January-February 2018. During this period, the easterly trade winds were interrupted for several days by coherent packages of rapidly descending air parcels reaching from the mid-latitude jet stream region into the cloud and sub-cloud layer close to Barbados. As those air parcels originate from the upper troposphere, they are anomalously dry and cold for the trade wind region. Therefore, they have a notable impact on diabatic processes in the vicinity of the trade wind cloud tops such as longwave cooling and cloud evaporation and sublimation. To quantify the Lagrangian heat budget along the dry intrusion, we performed a simulation with the Integrated Forecasting System (IFS, 0.4° horizontal resolution, 137 vertical levels) from the European Centre for Medium Range Weather Forecasts (ECMWF) with diabatic heating rate (DHR) output. We calculated backward trajectories based on hourly three-dimensional wind fields and analysed the DHR along the dry intrusion trajectories. In the first part of their descent from the mid-tropospheric jet stream region, the dry intrusion air parcels' heat budget is dominated by adiabatic warming. When arriving at the top of the moist boundary layer, the dry intrusion air parcels moisten and cool diabatically, due to radiative, turbulent and microphysical processes. This leads to cross-isentropic flow, which allows these air parcels to penetrate into the boundary layer. Thereafter, they experience strong diabatic warming by turbulent fluxes. Compared to typical airstreams in the trade wind region travelling from the east over the Atlantic on a constant pressure level, the analysed dry intrusion airstreams are special regarding their vertical motion associated with strong adiabatic temperature tendencies. The presented detailed case study thus illustrates, how the rapidly descending extratropical dry intrusion air is modified by the parametrised subgrid-scale processes when entering the boundary layer in the model, thereby affecting the thermodynamic conditions in the vicinity of low-level clouds.

# Contents

# 1 Introduction

In the trade wind region, low-level clouds cover about a third of the ocean surface (Nuijens et al., 2014). These clouds have a high impact on the climate by regulating the earth's radiative budget (Medeiros and Nuijens, 2016). The trade wind cloud cover consists of two cloud populations with a distinct daily cycle (Vial et al., 2019). Figure 1 schematically shows the typical vertical structure of the marine boundary layer and the two cloud populations. Shallow cumulus clouds with cloud base near the lifting condensation level (LCL) at about 925 hPa account for two thirds of the cloud cover (Nuijens et al., 2014, 2015). These mostly non-precipitating clouds form during the day (Vial et al., 2019) and show relatively small variance on time-scales longer than a day. Higher clouds contribute to one third of the trade wind cloud cover (Nuijens et al., 2014). These clouds mostly grow during the night and reach their maximum before sunset (Vial et al., 2019). In the mixed layer below the clouds the vertical profile is characterized by nearly constant potential temperature and specific humidity. At the top of the mixed layer relative humidity sharply decreases and potential temperature increases with height (Nuijens et al., 2015). Typically at around 750 hPa a stable layer marks the top of the highest clouds. This layer is called trade inversion (Nuijens et al., 2014).

Marine boundary layer clouds are at the heart of tropical cloud feedback uncertainties in climate models (Bony and Dufresne, 2005). While global climate models rely on parametrizations for the subgrid-scale clouds, high resolution models are bound to a limited model domain and are not able to cover variation in the large-scale circulation. Depending on the parametrization and model domains cloud properties differ between simulations with different models (Vial et al., 2017). In models with parametrized convection the low-level cloud cover is highly sensitive to the large-scale circulation. In contrast, the low-level clouds in high resolution models are nearly invariant to changes in the large-scale environment, which are expected in a warming climate (Vial et al., 2017). Fundamental puzzles of climate science remain unsolved because of our limited understanding of how clouds, circulation and climate interact (Bony et al., 2015). Therefore, the coupling between the trade wind cloud cover and the large-scale circulation is a key challenge to overcome uncertainties in future climate projections.

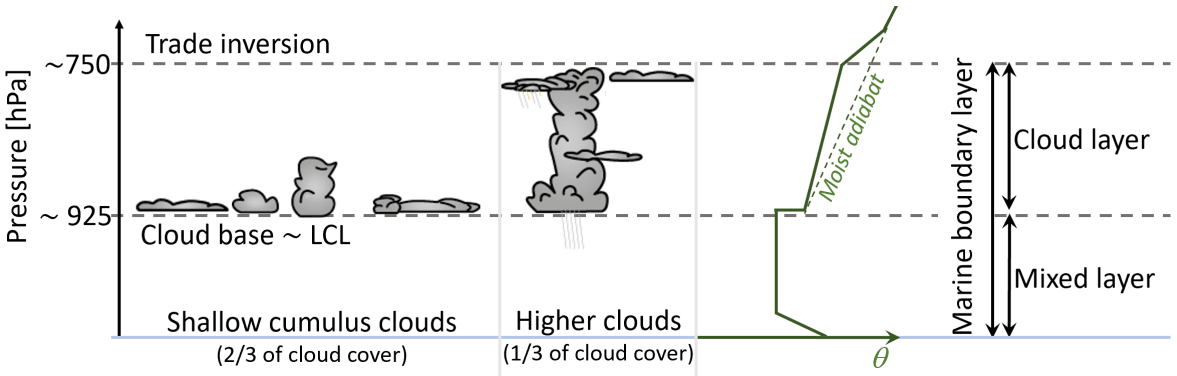


*Figure 1: Schematic of the marine boundary layer in the trade wind region showing the two cloud populations and the typical potential temperature profile (green).*

The large-scale circulation has an evident inuence on cloud formation (Bony et al., 2015). Low-level easterly winds with occasional intrusions of northeasterlies and large-scale subsidence aloft, associated with the Hadley and Ferrel cell, prevail in the wintertime north Atlantic trade wind region (Aemisegger et al., 2020). Figure 2a shows the north Atlantic cloud cover with a typical easterly flow situation in the trade wind region on 29 January 2018. On that day the shallow cumulus clouds in the western trade wind region shown in Fig. 2b feature a Gravel like structure (meso-scale cloud organisation pattern following Stevens et al. (2020)) with many cold pools developing (Aemisegger et al., 2020). However, the easterly flow is frequently interrupted by rapidly descending air parcels originating from the extratropics (Aemisegger et al., 2020). Such air parcels, with a descent of 300 to 400 hPa in 48 hours are called dry intrusions (DI) (Raveh-Rubin, 2017). Figure 2c and d show how the cloud cover over the Atlantic is influenced by a DI descending from the extratropics. In this flow regime, cloud free conditions prevail in the western trade wind region (Aemisegger et al., 2020).

DIs occur mainly in winter and typically travel from the extratropics equatorward (Raveh-Rubin, 2017). Starting their descent in the vicinity of the tropopause with low specific humidity, DIs bring relatively dry air into mid to lower tropospheric levels (Raveh-Rubin, 2017). In fact, dry air patches in the trade wind region mostly relate to DI-events (Yoneyama and Parsons, 1999). DI air masses affecting the western North Atlantic trade wind region almost exclusively originate in the Atlantic storm track region (Cau et al., 2007). They are often incorporated into the equatorward extension of tropospheric troughs, where they subside on the western side (Yoneyama and Parsons, 1999). DIs typically descend behind a cold front and fan out near the surface (Browning, 1997). In the western ocean basins over 70% of the DIs are associated with cold fronts (Catto and Raveh-Rubin, 2019). When occurring in combination with DIs, cold fronts are characterized by a larger frontal area with enhanced temperature gradients, frontal precipitation, wind gusts and ocean heat fluxes (Catto and Raveh-Rubin, 2019; Raveh-Rubin and Catto, 2019). DIs have also been shown to affect the duration and intensity of convection (Roca et al., 2005). The arrival of DIs at low levels can lead to a significant destabilization in the boundary layer accompanied by intensified surface fluxes, wind gusts and typically an increase of the boundary layer height (Raveh-Rubin, 2017).

The descent of a DI is overall close to adiabatic (Wernli, 1997; Raveh-Rubin, 2017). However, diabatic processes such as longwave radiation and evaporation of cloud condensate, when the DI approaches the cloud topped marine boundary layer, lead to a diabatic cooling of DI airmasses in the order of 3 K in two days (Raveh-Rubin, 2017). Towards the end of the descent phase the relative humidity of the airmass often increases, because of mixing in the moist boundary layer (Raveh-Rubin, 2017).

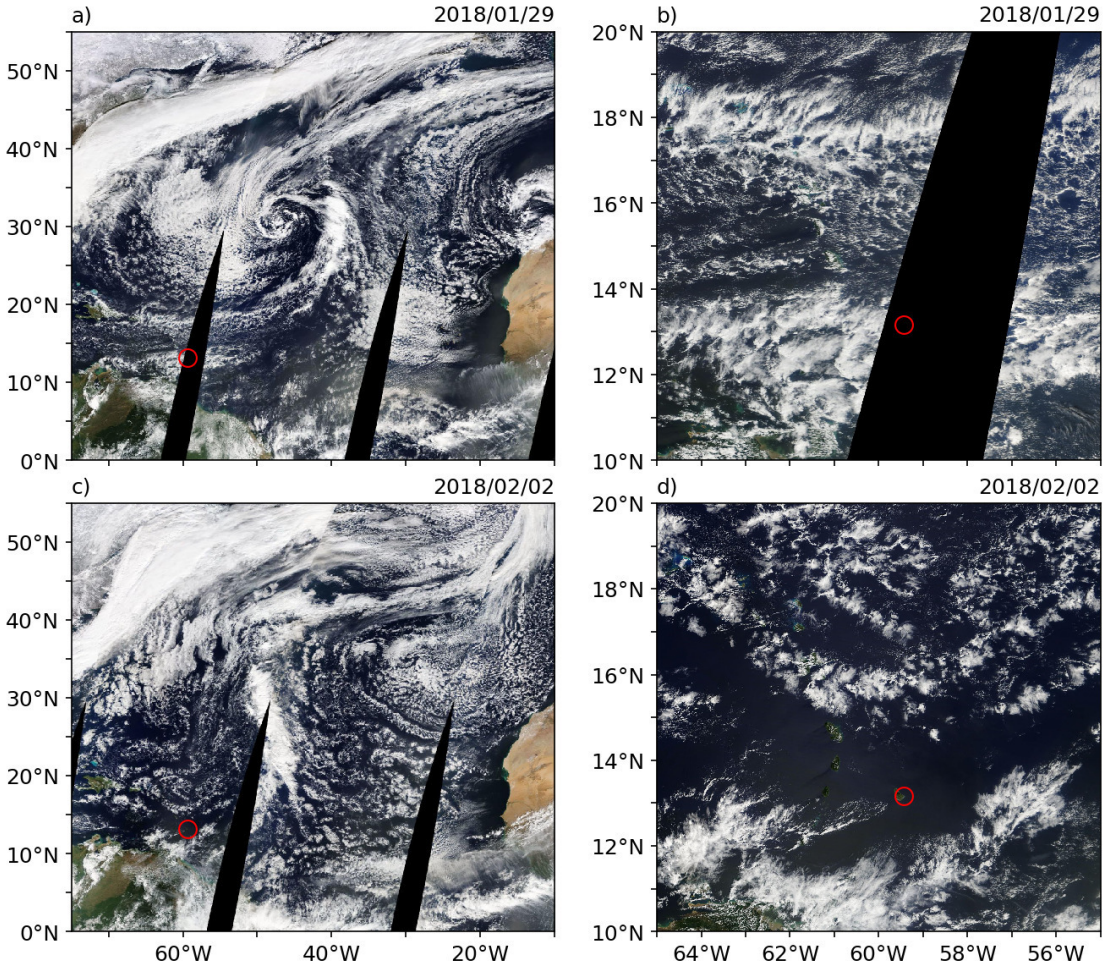


*Figure 2: Cloud patterns over the North Atlantic on a,b) 29 January and c,d) 2 February. Adapted from Aemisegger et al. (2020), with images from the MODIS instrument on the satellite Terra provided by NASA (https://wvs.earthdata.nasa.gov). The red circle marks the location of the Carribean Island Barbados.*

To address uncertainties in the trade wind region's low-level cloud cover and its impact on climate sensitivity, the extended field campaign EUREC$^4$A was launched in Barbados (Bony et al., 2017; Stevens et al., 2021). The cloud cover in Barbados has been shown to be representative for large parts of the tropical oceans (Medeiros and Nuijens, 2016). The 24 day pre-campaign isoTrades in winter 2018 focused on isotope measurements, giving insights in moisture sources of the low troposhere and their relation to the large-scale circulation (Aemisegger et al., 2020). Aemisegger et al. (2020) found an enhanced influence of DI occurrence in the second half of the isoTrade period. In the first part, the trade wind region flow is dominated by typical easterly winds bringing moist air from the eastern North Atlantic to Barbados.

In this thesis diabatic processes occurring along DI airmasses that reach Barbados during the IsoTrade period in 2018 are analysed in a Lagrangian framework. The methods are based on similar studies, that investigate the diabatic modification of air masses in extratropical weather systems, as conducted by Joos and Wernli (2012) for warm conveyor belts (WCB), by Attinger et al. (2019) for extratropical cyclones and by Spreitzer et al. (2019) for the tropopause region. The European Center for Medium-Range Weather Forecasts (ECMWF) Integrated Forecast System (IFS) with diabatic heating rates (DHR) as model output is used to quantify the impact of different parametrized processes, that affect the DI airmass. The aim is to increase our mechanistic understanding of the interaction between DIs and the parametrized diabatic processes, which modify the thermodynamic properties in the environment of the low-level clouds in the trade wind region.

The following questions will be addressed:

1. How did the large-scale weather situation during the isoTrades campaign influence airmasses arriving in Barbados in terms of origin and vertical motion along their path?

2. What are the dominant diabatic processes shaping the descent of a DI airstream?

3. How does a DI airstream interact with its environment and clouds when arriving at the top of the boundary layer? How does the DI airstream influence vertical gradients in specific humidity and temperature around the boundary layer top and how are the thermodynamic properties of the DI airstream modified when interacting with clouds?

4. How does a DI airstream differ from a typical trade wind airstream with regard to their thermodynamic history?

The thesis is organized as follows: In Sect. 2 the applied methods and the IFS data are described. Sect. 3.1 gives an overview of the synoptic situation. In Sect. 3.2 the influence of the synoptic situation on the transport pathways of air parcels reaching Barbados is analysed. This is followed by a detailed case study of two DI airmasses in Sect. 3.3 and two typical trade wind airmasses in Sect. 3.4. Sect. 3.5. compares and summarizes the processes affecting DI and the trade wind airstreams. A conclusion is given in Sect. 4.

# 2 Data and methods

## 2.1 The IFS model

The IFS, cycle 43R1 from the ECMWF is used to simulate a 13 day period in February 2018. The IFS is operated in a special version as part of the ECMWF special project "Diabatic effects in mid-latitude weather systems" [1], that enables additional output of the heating rates from all parametrized processes. The simulation is initialized on 24 January at 12 UTC from the ECMWF analysis field. The IFS runs on 137 vertical levels and at a cubic spectral truncation of TCo639, corresponding to roughly 16 km horizontal grid spacing. The model integration time step is 12 min. The hourly output variables used in the case study are interpolated to a regular grid at 0.4° horizontal resolution. Among others, clouds and large-scale precipitation, convection, radiation and turbulent transport are parametrized in the IFS as described in "IFS Documentation CY43R1 - Part IV: Physical Processes" (2016). Large-scale precipitation and large clouds are parametrized by the large-scale microphysics scheme, with prognostic equations for water vapour, cloud water, cloud ice, rain and snow water contents. Fig. 3 shows a schematic of the processes that are parametrized in the IFS large-scale microphysics scheme.

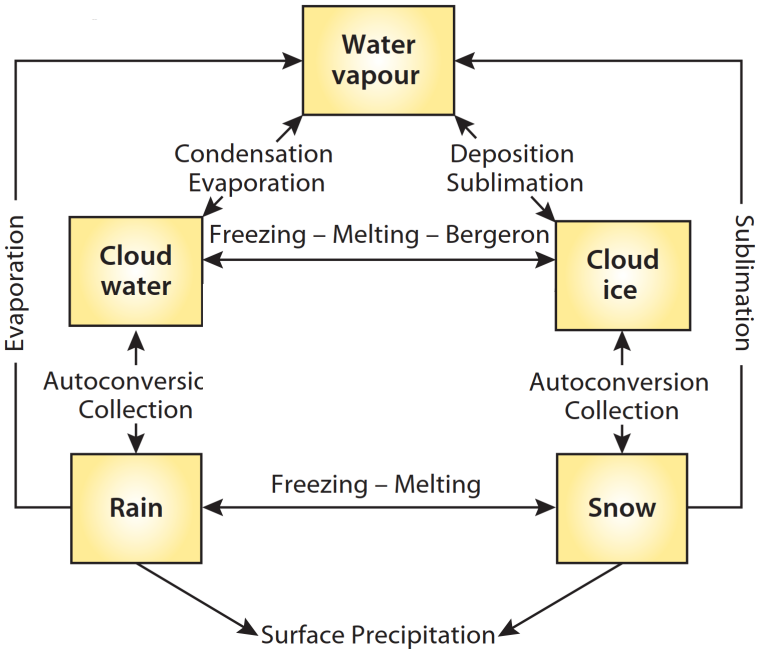


*Figure 3: Schematic of the IFS large-scale microphysics scheme, adapted form "IFS Documentation CY43R1 - Part IV: Physical Processes" (2016). Yellow boxes indicate prognostic variables.*

[1] https://www.ecmwf.int/en/research/special-projects/spchbojo-2018

| Abbreviation: | Diabatic heating rate (DHR) for physical process: |
|---|---|
| $DHR_{ls}$ | from the large-scale microphysics scheme |
| $DHR_{conv}$ | from the convective scheme |
| $DHR_{turb}$ | from vertical diffusion and drag schemes (turbulent temperature exchange) |
| $DHR_{lw}$ | from long-wave radiation |
| $DHR_{sw}$ | from short-wave radiation |
| $DHR_{cond}$ | Condensation of water vapour |
| $DHR_{evc}$ | Evaporation of cloud water |
| $DHR_{evr}$ | Evaporation of rain |
| $DHR_{dep}$ | Depositional growth of ice |
| $DHR_{melts}$ | Melting of snow |
| $DHR_{melti}$ | Melting of cloud ice |
| $DHR_{subs}$ | Sublimation of snow |
| $DHR_{subi}$ | Sublimation of ice |
| $DHR_{frz}$ | Freezing of cloud droplets |
| $DHR_{rime}$ | Riming of cloud droplets |

*Table 1: Overview of all DHRs given in the hourly IFS output. The lower row corresponds to the microphysical processes, that contribute to the $DHR_{ls}$.*

## 2.2 Diabatic temperature and moisture tendencies from the IFS model

Potential temperature is materially conserved in the absence of diabatic processes. The latter processes are typically assosiated with smaller scales than the model grid, hence they are parametrized in the IFS. The parametrized processes effect the potential temperature by diabatic heating or cooling. The special IFS version provides instantaneous DHRs from each individual parametrized process. Following Joos and Wernli (2012) the effect of the individual DHRs on the total diabatic heating $DHR_{diab}$ is analysed in a Lagrangian framework. Equation 1 summarizes in detail the physical processes contributing to $DHR_{diab}$. The diabatic processes considered in this study are listed in Table 1.

$$DHR_{diab} = DHR_{ls} + DHR_{lw} + DHR_{sw} + DHR_{conv} + DHR_{turb} \tag{1}$$

$DHR_{ls}$ sums latent heating and cooling associated with clouds and large-scale precipitation, which are computed in the large-scale microphysics scheme. Changes in water vapour, cloud water, cloud ice, rain and snow water content resulting in latent heat release or consumption are listed in the lower row of table 1. $DHR_{lw}$ and $DHR_{sw}$ are the longwave and shortwave radiative heating rates. The convection term $DHR_{conv}$ adds heating rates from unresolved cloud microphysical processes associated with unstable air parcels. $DHR_{turb}$ represents the temperature tendency due to turbulent heat exchange from the vertical diffusion and the orographic drag schemes (Spreitzer et al., 2019).

Some of the diabatic processes mentioned before also modify the humidity. Changes in specific humidity ($\Delta q$) result from moistening or drying due to subgrid-scale convection ($\Delta q_{conv}$), turbulence ($\Delta q_{turb}$) or large-scale microphysical processes ($\Delta q_{ls}$). The humidity

tendency of each process is given as an hourly output in the IFS. The sum of the individual humidity tendencies results in the total change of specific humidity ($\Delta q_{diab}$), as seen in equation 2.

$$\Delta q_{diab} = \Delta q_{conv} + \Delta q_{turb} + \Delta q_{ls} \tag{2}$$

## 2.3 Trajectory calculation

For the period between 29 January and 6 February 2018 five-day backward trajectories are calculated. The Lagrangian Analysis Tool LAGRANTO (Wernli, 1997; Sprenger and Wernli, 2015) is used for the trajectory calculation. It is based on the three-dimensional hourly wind field from the IFS simulation. The trajectories are started hourly at the Barbados Cloud Observatory (BCO) (13.16°N, 59.43°W) and at four additional points surrounding BCO (0.5° displaced zonally and meridionally). The starting points are vertically stacked every 5 hPa between sea level pressure and 550 hPa. Around 460 trajectories are calculated for every hour time step (the exact number depends on the sea level pressure). Besides other variables, the three-dimensional DHRs and $\Delta q$ are traced along the trajectories.

## 2.4 Categorization of trajectories and selection of airstreams

As the calculated trajectories have different origins and thus distinct individual thermodynamic histories, a joint analysis of the diabatic tendencies of all trajectories is not insightful. We therefore group the trajectories in 13 categories by combining the four criteria listed below. The categorization later helps to select interesting bundles of trajectories for further analysis.

1. The arrival pressure level at the BCO: We distinguish trajectories arriving above cloud top from those arriving below. As in Aemisegger et al. (2020), we define the cloud top of the trade wind cumuli at 700 hPa. This is slightly above the typical level of the wintertime trade wind inversion in Barbados at around 750 hPa (Medeiros and Nuijens, 2016).

2. The maximal latitude reached by the trajectory: We differentiate between extratropical trajectories reaching higher latitudes than 30°N, subtropical trajectories reaching between 23°N and 30°N and tropical trajectories, which are permanently to the south of 23°N.

3. The maximal descent in two days: DI trajectories can be selected by their strongest descent in two days (Wernli, 1997; Raveh-Rubin, 2017). We use the criterion of 300 hPa in two days to select DI's. This is slightly less strong than in Raveh-Rubin (2017), who used a minimal descent of 400 hPa in two days as a threshold. The criterion chosen here is a trade-off between ensuring strong descent, while having a representative number of trajectories selected. We further used the threshold of 200 hPa in two days, to distinguish between rapidly descending and more moderately descending airstreams.

4. The maximal ascent in two days: We used the criterion of 300 hPa ascent in two days to detect strong ascent for airstreams that rapidly ascended before descending

again. The chosen criterion is weaker than for warm conveyor belts as defined by Madonna et al. (2014). Nevertheless, we will refer to this airstream as a WCB-DI, due to its WCB-like ascent into the jet before the rapid subsidence into the tropics.

To further investigate the thermodynamic history of air parcels in different categories, bundles of at least ten coherent trajectories are selected. These coherent packages of air parcels will be referred to as airstreams. Having multiple trajectories in the defined airstreams leads to a statistically more robust signal in the DHRs. This approach increases our confidence in trajectories especially in regions, where subgrid-scale turbulence affects the wind field and can lead to uncertainties in the resolved wind.

## 2.5 Partitioning of the temperature tendencies and residual

Four selected airstreams are analyzed in terms of their temperature tendencies. As an additional diagnostic to the DHRs introduced in Sect. 2.2, we also apply a distinction between diabatic and adiabatic temperature change along the trajectories. The method is based on the thermodynamic energy equation and follows Bieli et al. (2015) and Hermann et al. (2020). From the thermodynamic energy equation and the material derivative of potential temperature, we can write eq. 3, which relates temperature changes to adiabatic air mass movement (cooling due to adiabatic ascent and warming due to adiabatic descent). The first term on the right, is the adiabatic temperature tendency, $\Delta T_{adiab}$. Here, $\omega$ is the vertical velocity in pressure coordinate, $\omega = \frac{Dp}{Dt}$. $\kappa$ equals to $R/cp = 287$, with the gas constant of dry air $R = 287\,\mathrm{J\,(K\,kg\,)^{-1}}$ and the specific heat capacity $cp = 1005\,\mathrm{J\,(K\,kg)^{-1}}$. The second term in eq. 3 accounts for the diabatic heating. Here, $\frac{D\Theta}{Dt}$ is the material change in potential temperature and $p_0$ the reference pressure.

$$\frac{DT}{Dt} = \Delta T_{adiab} + \Delta T_{diab} = \frac{\omega \kappa T}{p} + \frac{D\Theta}{Dt}(p_0/p)^{\kappa} \tag{3}$$

To compare their relative contribution, the diabatic and the adiabatic term are calculated separately. The diabatic term is discretised as in eq. 4, with $\Delta$ t = 1 hour.

$$\Delta T_{diab,t} = \frac{\Theta_t + \Theta_{t-1}}{\Delta t}\left(\frac{2p_0}{p_t + p_{t-1}}\right)^{-\kappa} \tag{4}$$

The adiabatic term is calculated from the diagnosed difference between $\frac{DT}{Dt}$ and $\Delta T_{diab}$. Note that $\Delta T_{diab}$ corresponds to the sum of the individual DHRs from eq. 1 including a residual $RES_{DHR}$ :

$$\Delta T_{diab} = DHR_{diab} + RES_{DHR} \tag{5}$$

A residual can arise from using hourly instantaneous DHRs, because constant DHRs are assumed over five internal model time steps. According to Spreitzer et al. (2019) the use of accumulated DHRs instead of instantaneous DHRs at the time of the model output does not lead to a reduction of the residual. When evaluating DHRs in a Lagrangian perspective, position errors may additionally arise from the trajectory calculation. This can lead to a residual resulting from linear interpolation (Spreitzer et al., 2019). However, if the $RES_{DHR}$ is small compared to $\Delta T_{diab}$, we can safely assume that the DHRs adequately represent the diabatic processes in the airstream.

# 3 Results

## 3.1 Large-scale weather situation during the isoTrade dry intrusion event

The large-scale weather situation during January and February 2018 over the central Atlantic was strongly influenced by the formation of a stratospheric cutoff (isolated region of stratospheric air associated with cyclonic rotation beneath). This cutoff was formed during an anticyclonic Rossby wave breaking event between 25 and 29 January over the central North Atlantic. On 26 January, an upper level ridge is located over the central Atlantic (Fig. 4a, around 50°N, 50°W). During the following two days an elongated PV

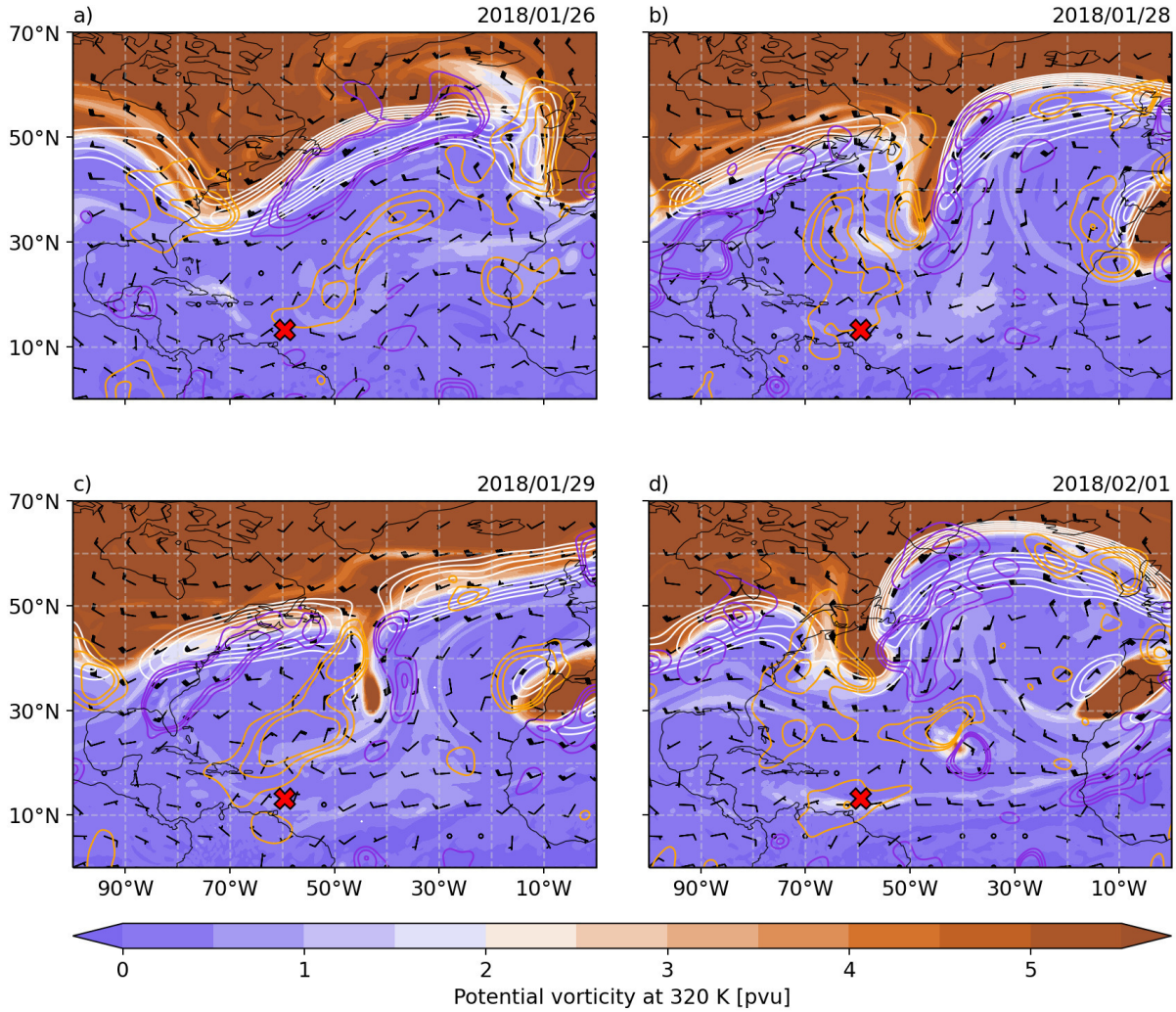


*Figure 4: Atmospheric flow condition at 320 K at 00 UTC on a) 26 January, b) 28 January, c) 29 January and d) 1 February. PV (colors), horizontal wind speed (white contours from 40 to* $70\,\mathrm{m\,s^{-1}}$ *in steps of* $5\,\mathrm{m\,s^{-1}}$*), wind barbs (black), vertical wind* $\omega$ *(orange contours for descent 0.1, 0.15 and* $0.2\,\mathrm{Pa\,s^{-1}}$ *and purple contours for ascent -0.1,-0.15 and* $-0.2\,\mathrm{Pa\,s^{-1}}$*). The red cross indicates the position of Barbados (BCO). The* $\omega$ *contours are smoothed with a Gaussian filter for better readability.*

filament (PV streamer) forms over the same area (Fig. 4b). On 29 January, in the final stage of the Rossby wave breaking event, the PV streamer develops into a stratospheric cutoff (Fig. 4c, 35°N, 43°W). In the following days, the cutoff moves southeastward, until it decays in the second half of 1 February, near 25°N, 40°W (Fig. 4d). The presence of this relatively persistent cutoff low over the central North Atlantic was a key ingredient in the formation of the isoTrades DI.

The atmospheric flow condition over the central Atlantic on 26 January (Fig. 5a,b), before the formation of the stratospheric cutoff, is different than after this event on 29 January (Fig. 5b,c). On 26 January a trough is building along the eastern North American coast (Fig. 5a). This trough will later develop into a PV streamer, which will form the

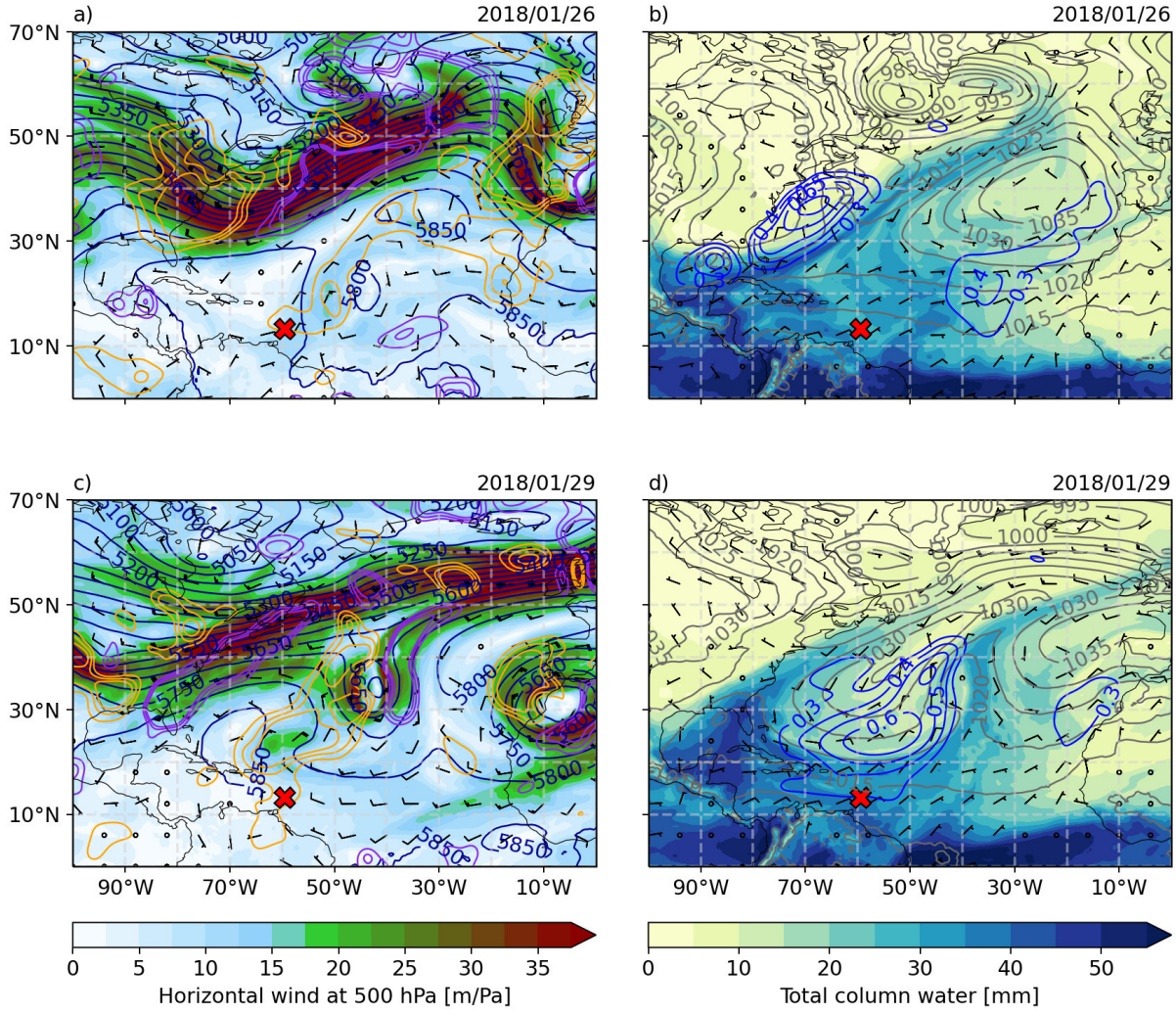


*Figure 5: Low and mid level atmospheric flow condition at 00 UTC on a,b) 26 January and c,d) 29 January. a,c) Wind field at 500 hPa: horizontal wind speed (colors), wind barbs (black), vertical wind $\omega$ (orange contours for descent 0.1, 0.15 and $0.2\,\mathrm{Pa\,s^{-1}}$ and purple contours for ascent -0.1,-0.15 and $-0.2\,\mathrm{Pa\,s^{-1}}$), geopotential height [m] at 500 hPa (blue contours). b,d) Total column water content (colors), surface pressure [hPa] (grey contours) and surface evaporation [mm/h] (blue contours). The red cross indicates the position of Barbados (BCO). The $\omega$ and surface evaporation contours are smoothed with a Gaussian filter for better readability.*

cutoff. The low-level wind field on 26 January is dominated by a quasi-stationary high pressure system over the Azores (Fig. 5b). In the trade wind region, easterly winds dominate. In the extratropics on the western side of the heigh pressure system, southwesterly winds bring moist air to higher latitudes. On 29 January, the cutoff low forms and the associated low-level cyclonic flow in the central North Atlantic strengthens (Fig. 5b, 35°N, 40°W). At 500 hPa the subsidence and cyclonic wind field increase around a large-scale region of enhanced descent on the western side of the cutoff low and the surface cyclone. The descent region is linked to the stratospheric PV anomalies, which are induced by the PV streamer and upheld by the stratospheric cutoff. Positive PV anomalies over a baroclinic zone typically induce quasi geostrophic subsidence on their western side. The coupling between the positive upper level PV anomaly and the surface low pressure system induce a cyclonic flow throughout the troposphere on 29 January (Fig. 5d). Thus, the resulting wind field on the western side of the cutoff is southward and descending. This is important to steer extratropical DI airmasses toward Barbados (see Sect. 3.2). The total column water content in that region is low, due to the slantwise advection of dry air from the midlatitude upper troposphere. North of Barbados, at 20°N, a strong horizontal gradient in total column water content marks the position of the cold front. Behind the cold front, to the west and southwest of the surface low pressure system, surface evaporation is strongly enhanced, an effect that is induced by the northerly flow and the turbulent mixing of dry air into the boundary layer.

To conclude this section, on 29 January a stratospheric cutoff forms over the central Atlantic. Coupled to a surface low pressure system, it induces enhanced descent and southward motion on its western side. This brings dry extratropical air from the north west of the cutoff into the trade wind region southwest of the cutoff. The arrival of dry air in the low-level trade wind region amplifies ocean evaporation beneath.

## 3.2 Airstreams reaching Barbados before and after the formation of the stratospheric cutoff

The calculated backward trajectories show the influence of the stratospheric cutoff on the origin of air parcels in Barbados. The relation between anticyclonic Rossby wave breaking, leading to the formation of the cutoff and the origin of air parcels arriving in the western Nord Atlantic trade wind region in winter 2018 is established in Aemisegger et al. (2020).

In Fig. 6a trajectories arriving on 30 January are shown. These trajectories are barely influenced by the stratospheric cutoff, which only formed shortly before their arrival on 29 January and their pathway follows the typical easterly trade wind flow. The position of the trajectories on 26 January as well as their arriving pressure level is indicated by coloured points. Trajectories arriving in the sub-cloud layer (below 940 hPa) on 30 January are mostly of subtropical origin and are advected isobarically from the eastern coast of Africa. Parts of the trajectories arriving in the cloud layer (between 940 hPa and 700 hPa) are of tropical origin and also move isobarically towards the West. A few trajectories descent from the central North Atlantic above 600 hPa to Barbados.

Trajectories arriving on 2 February in Barbados have been influenced by the presence of the central North Atlantic cutoff and show an altogether completely different pathway from the ones arriving on 30 January (Fig. 6b). Air parcels arriving in the sub-cloud layer

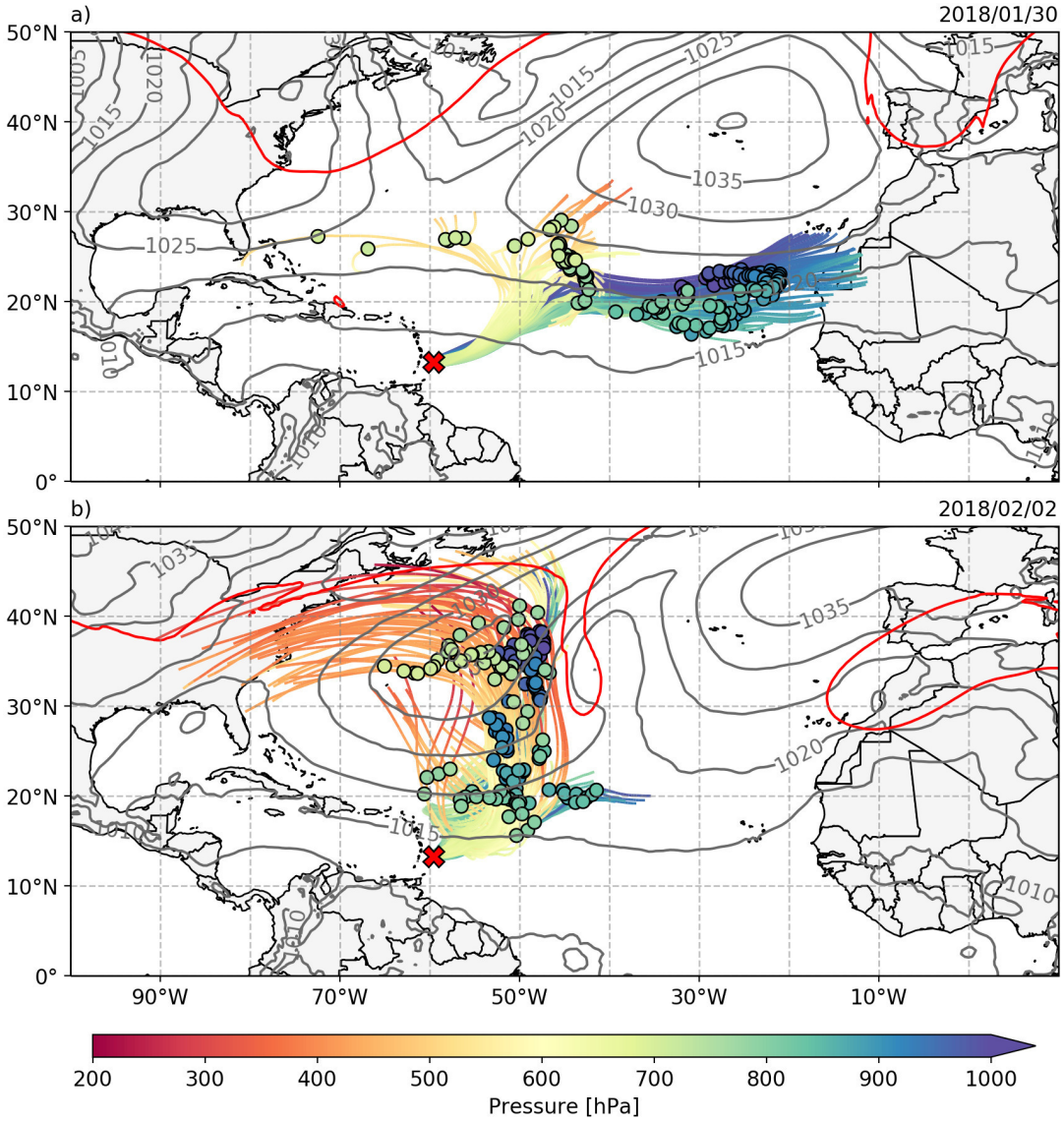


*Figure 6: Backward trajectories starting below 700 hPa from Barbados (BCO) at 00 UTC on a) 30 January and b) 2 February. The trajectories are coloured according to their pressure. Sea level pressure [hPa] (grey contours) and the 2 pvu tropopause at 320 K (red contour) are given four days before arrival on a) 26 January and b) 29 January. The trajectories' position at that time is indicated by dots, coloured by their arrival pressure. The red cross indicates the location of Barbados (BCO).*

and most of the trajectories arriving in the cloud layer originate from the extratropics. Most often they follow the midlatitude jetstream and descend on the western side of the trough. On 29 January the trajectories are located on the western side of the stratospheric cutoff in a region of enhanced subsidence and southward motion (see Sect. 3.1). At that time, the trajectories exhibit a strong descent towards the trade wind region. Thereafter, they move on the eastern side of a surface anticyclone to Barbados. Only a few trajectories arriving on 2 February are of tropical origin.
The origin of all air parcels as defined by the criteria in Sect. 2.4 is shown in terms of trajectory number for the entire simulation in Fig. 7. Until 00 UTC on 31 January nearly all the trajectories arriving in the cloud and sub-cloud layer (below 700 hPa) are of tropical or subtropical origin (Fig. 7a). Above 700 hPa the air parcels are mostly coming from the extratropics (Fig. 7b). Some of them are strongly descending. However, these strongly descending trajectories arrive above the trade inversion. They are barely influenced by the stratospheric cutoff, which formed on 29 January, when these air parcels are already close to Barbados. Detailed case-studies of a tropical (darkblue in Fig. 7a) and a subtropical (turquoise in Fig. 7a) airstream arriving at 21 UTC on 29 February below 700 hPa follows in Sect. 3.4.

From 31 January on, the number of tropical trajectories decreases. Instead extratropical trajectories, some of them strongly descending, arrive in the cloud or sub-cloud level (Fig. 7a). On 31 January and 1 February a large number of DI trajectories arrive below 700 hPa (darkred in Fig. 7a). Also, a few trajectories arriving above cloud top exhibit a phase of strong WCB-like ascent before subsiding (red in Fig. 7b). The DHRs along two selected airstreams, that belong to these categories are analysed in in Sect. 3.3. After 2 February nearly no tropical trajectories arrive at the BCO. Trajectories arriving at low levels are mostly descending from the extratropics or, in the night to 4 February, from the subtropics.

In summary, before 31 January trajectories arriving at low levels are predominately of tropical and subtropical origin. Thereafter, with the formation of the stratospheric cutoff and a cyclone beneath it in the central North Atlantic, the number of trajectories descending from the extratropics into the trade wind region increases. This increase relates to the extended area of strong descent and southward wind direction to the west of the stratospheric cutoff.

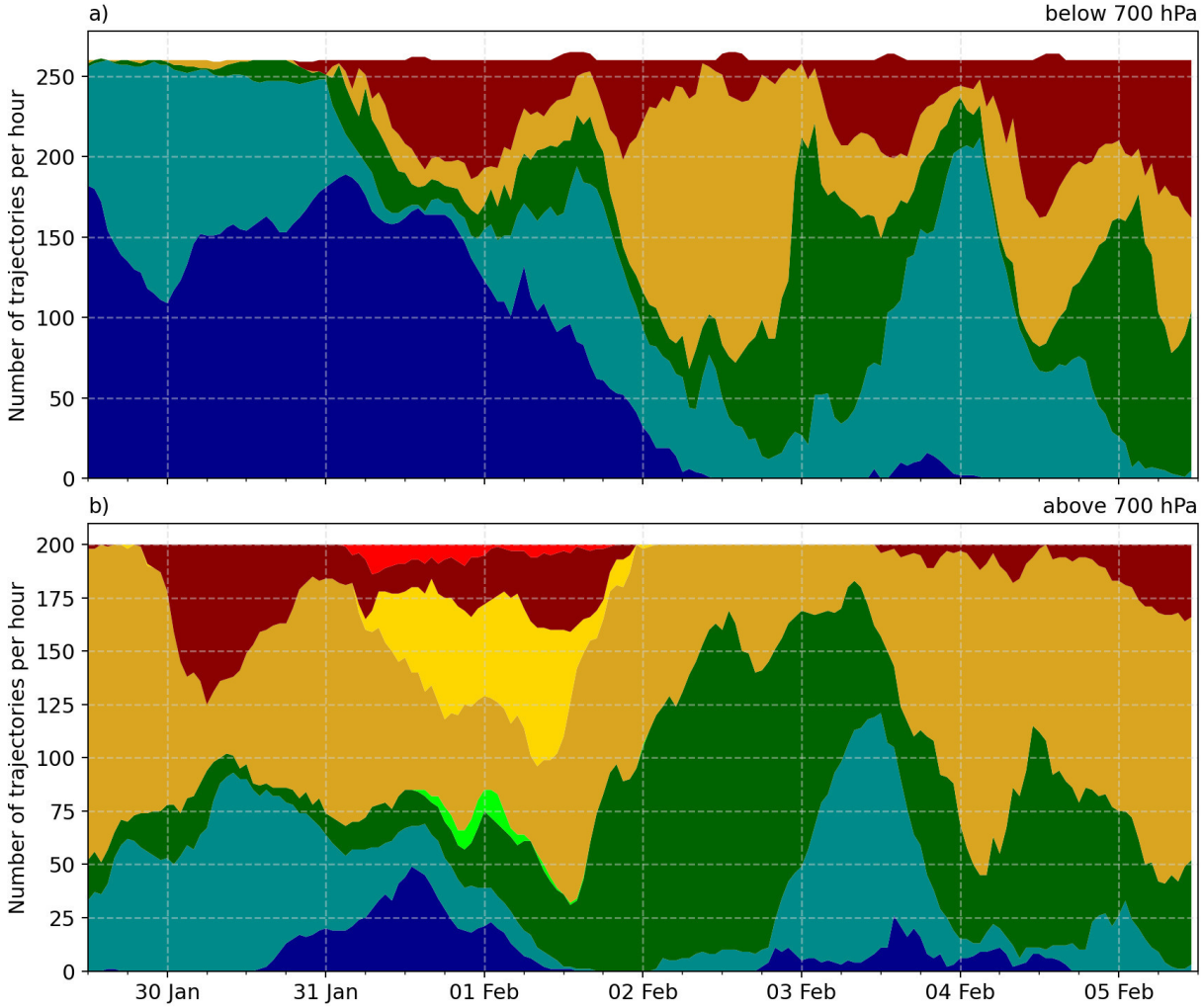


| | Max. reached latitude | Max. descent in 48 h | Max. ascent in 48 h >300 hPa |
|---|---|---|---|
| | >30°N | >300 hPa | yes |
| | | | no |
| | >30°N | <300 hPa & >200 hPa | yes |
| | | | no |
| | >30°N | <200 hPa | yes |
| | | | no |
| | <30°N & >23°N | | |
| | <23°N | | |

*Figure 7: Number of hourly calculated backward trajectories arriving a) below 700 hPa and b) above 700 hPa, with the starting time from BCO on the x-Axis. Colours indicate the properties of the trajectories as indicated in the table.*

## 3.3 Dry intrusion airstreams

This section treats two selected airstreams that arrive at the beginning of the DI's influence, at 21 UTC on 31 January, in Barbados. Their most important segments are described along with the relevant diabatic heating processes.

### 3.3.1 Case study "WCB-DI-above"

The airstream "WCB-DI-above" is a special airstream given its pathway associated with considerable vertical motion. It includes relatively few trajectories (11), which belong to the red category in Fig. 7b. Their coherent path can be split into three segments: a rapid ascent phase in a cloudy environment, a strong descent in a dry environment and the arrival at the cloud top near Barbados. In the following the three segments are described in detail.

**Ascent segment in mixed phase clouds:** On 27 January the airstream starts above the Gulf of Mexico below 800 hPa, where it ascends rapidly within a WCB (Fig. 8). In this region WCBs are relatively frequent in winter (Madonna et al., 2014). During the ascent the airstream follows the lower part of the midlatitude jetstream for 2 days. To understand diabatic processes along the trajectories (shown in Fig. 9b-d), it is important to consider the airstreams environment. The average profile along the path of the airstream is shown in Fig. 9a. For every "WCB-DI-above" trajectory a vertical profile of the thermodynamic conditions of the atmosphere is taken hourly at its horizontal location. The resulting 11 (the number of trajectories in the airstream) 2D timeseries are then averaged. The vertical profile of the DHRs is shown in a similar way in Fig. 9b with contours marking

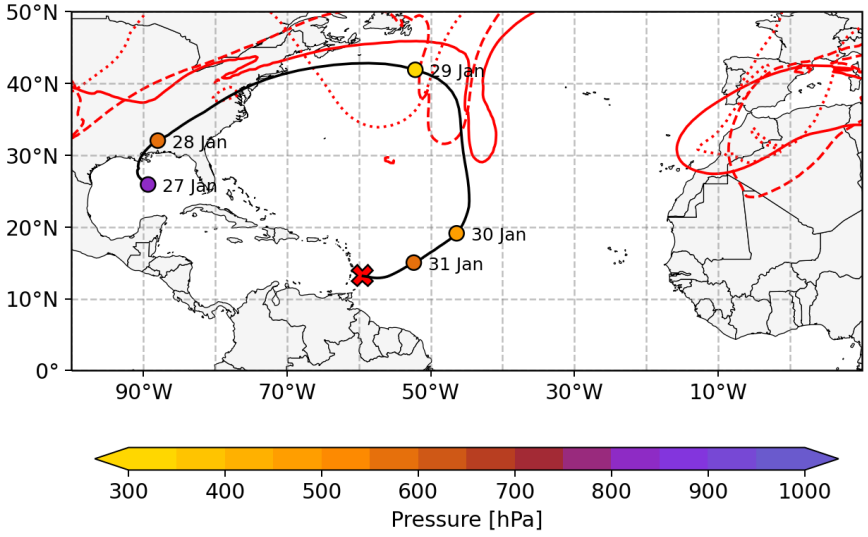


*Figure 8: Path of the "WCB-DI-above" airstream. The median location of the trajectories is indicated by dots every day at 00 UTC, coloured according to the pressure level. The* 2 pvu *tropopause on* 320 K *is shown at 00 UTC on 27 January (red dotted contour), 28 January (red dashed contour) and 29 January (red solid contour). The red cross indicates the location of Barbados (BCO).*

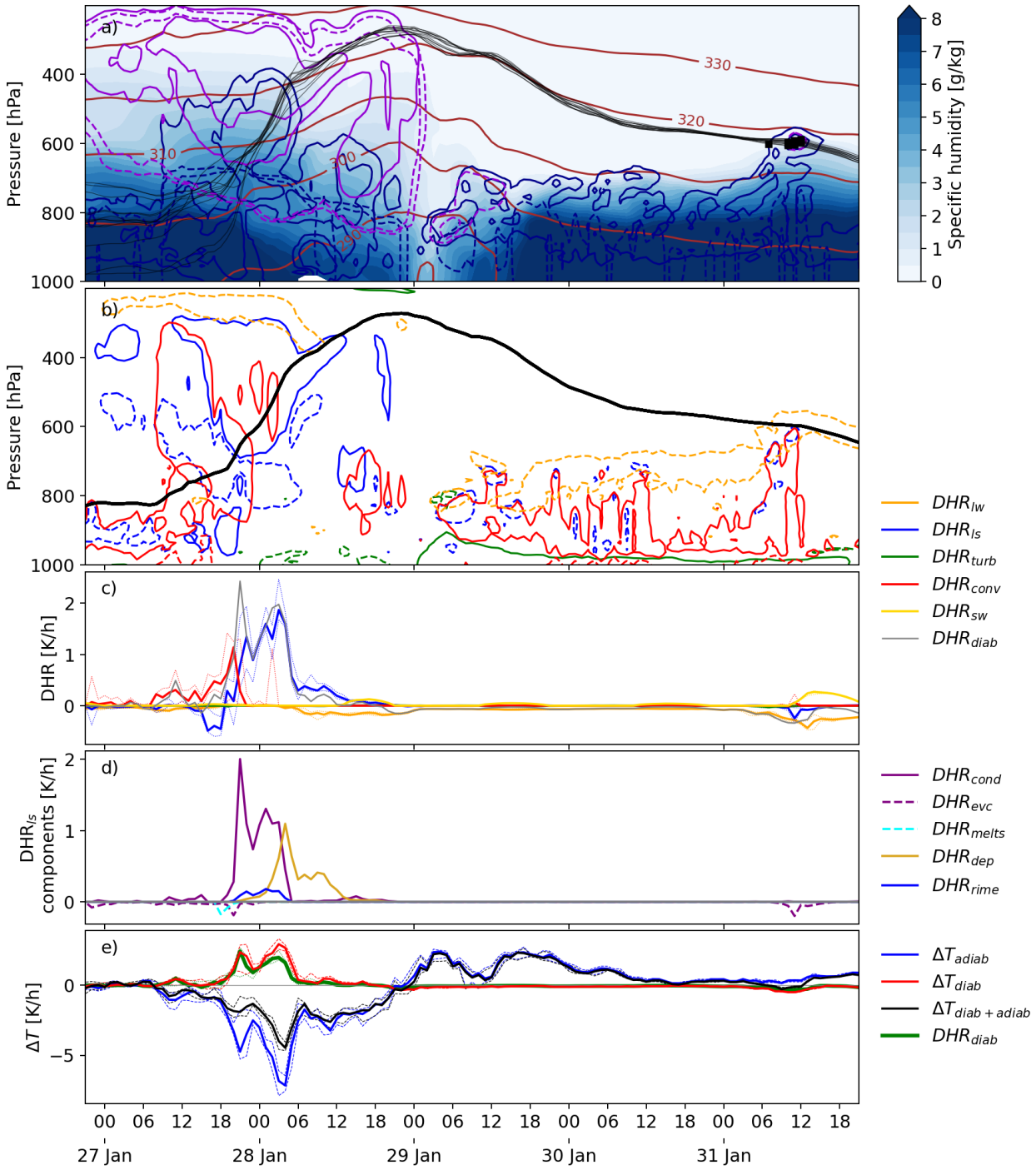


*Figure 9: a,b) Mean vertical cross sections along the "WCB-DI-above" airstream. a) Trajectories (black lines), specific humidity (shading), cloud and ice water content (blue and purple solid contours for 10 and 50 mg kg$^{-1}$), rain and snow water content (blue and purple dashed contours for 1 and 5 mg kg$^{-1}$) and potential temperature [K] (brown contours). b) DHRs (solid contours for 0.2 K h$^{-1}$ warming and dashed contours for −0.2 K h$^{-1}$ cooling) and the median of the trajectories' position (black). c) DHRs at the airstreams' location. d) $DHR_{ls}$-components reaching absolute values bigger than 0.01 K h$^{-1}$. e) Partitioning of the temperature tendencies as described in Sect. 2.5. The difference between $\Delta T_{diab}$ and $DHR_{diab}$ is the residual term. Solid lines in c, d and e mark the median and dashed lines the 0.25 and 0.75 quantiles.*

regions where DHR components reach rates above $0.2\,\mathrm{K\,h^{-1}}$ (solid contours) or below $-0.2\,\mathrm{K\,h^{-1}}$ (dashed contours).
The ascent during the first 2 days is accompanied by strong adiabatic cooling. This can be seen in Fig. 9e, which shows the partitioning into diabatic and adiabatic temperature tendencies, as described in Sect. 2.5. When saturation is reached and condensation starts to occur, latent heat release leads to a diabatic warming (see heating rates by convection in red and large-scale microphysics in blue in Fig. 9b,c). The diabatic warming causes cross-isentropic ascent (see the vertical crossing of isentropes in Fig. 9a) and thereby further increases the adiabatic cooling (Fig. 9e). Between 17 and 21 UTC on 27 January, the airstream is influenced by snow and rain falling from clouds above, that presumably relate to air parcels ascending ahead of the analysed airstream. This leads to a short time cooling effect from the cloud microphysics scheme, caused by melting and evaporation in the warm, partly subsaturated air parcels (see Fig. 9d). Further aloft clouds again form along the WCB's ascent pathway. These are associated with the well-known cloud band that can be observed along the cold front of extratropical cyclones (Joos and Wernli, 2012). In the mixed phase clouds the large-scale microphysics scheme warms the airstream primarily by condensation (Fig. 9d). Riming (the collection of supercooled droplets by ice crystals) has an additional warming effect. Closer to the cloud top, deposition (desublimation on cloud ice) becomes the dominant heating process.

**Descent segment in a dry environment:** At 21 UTC on 28 January, the airstream reaches its maximal height above 400 hPa and starts descending (Fig. 8, 9). The air parcels thereby move out of the WCB ice cloud and start their descent on the right exit of a jet streak in a dry environment. On 29 January the airstream is located westward of the stratospheric cutoff, where it descends strongly. During the descent, longwave radiation cools the airstream by about $-0.05\,\mathrm{K\,h^{-1}}$ (see Fig. 9c). At local noon, when the shortwave radiation is maximal it offsets the longwave cooling. However, the diabatic cooling during the descent is small compared to the adiabatic warming (Fig. 9e). On 30 January the airstream reaches into the tropics, where it merges with the trade wind flow (see westward path in Fig. 8). Here, the subsidence of the airstream slows down, which shows in a reduced adiabatic warming (Fig. 9e).

**Arrival at cloud top:** At 11 UTC on 31 January the airstream reaches the top of a mixed phase cloud, slightly above 700 hPa close to Barbados (Fig. 9). At cloud top the longwave radiative cooling increases and cloud evaporation adds to the diabatic cooling (Fig. 9b,c). This increased diabatic cooling locally offsets the adiabatic warming (Fig. 9e) and leads to an increased descent rate shortly before the arrival at the BCO.

### 3.3.2 Case study "DI-below"

The "DI-below" airstream descends from the free troposphere in the extratropics into the trade wind region's sub-cloud layer. It consists of 39 trajectories that belong to the darkred category in Fig. 7a. Their path can be described in three parts: a descent segment in the free troposphere, the penetration into the boundary layer and a descent segment in the boundary layer. The exact time when the trajectories penetrate into the boundary layer differs between the trajectories. To better understand the timing and and magnitude

of the diabatic processes along individual trajectories, a single representative trajectory is selected for the description of the two descent segments and to show the airstreams environment at the time step when it arrives at the top of the boundary layer. At the end of this section, composites are used to summarize all the 39 trajectories at this time step.

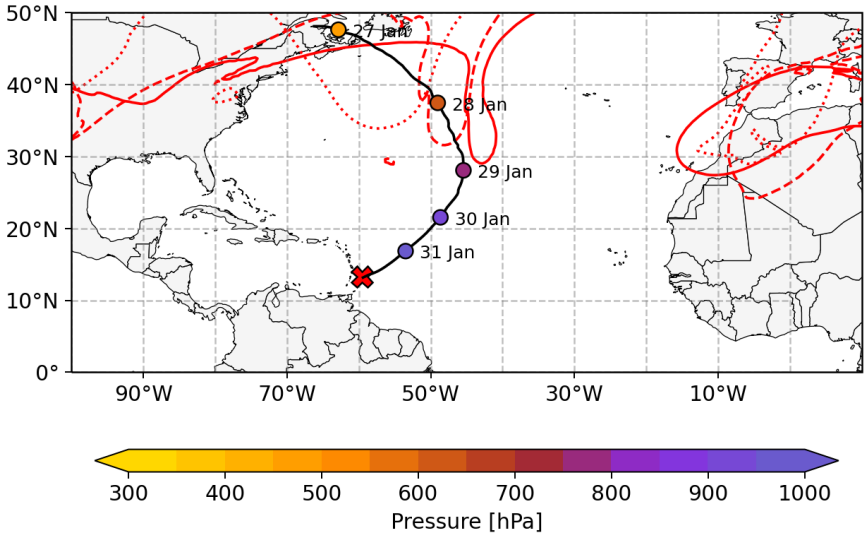


*Figure 10: Path of the selected trajectory from the "DI-below" airstream. The location of the trajectory every day at 00 UTC is indicated by dots coloured according to the pressure level. The 2 pvu tropopause on 320 K is shown at 00 UTC on 27 January (red dotted contour), 28 January (red dashed contour) and 29 January (red solid contour). The red cross indicates the location of Barbados (BCO).*

**Descent segment in the free troposphere:** Between 27 January and 29 January the airstream descends and travels southeastwards (Fig. 10). Compared to the "WCB-DI-above" airstream the "DI-below" airstream starts its descent at a lower altitude, where it is influenced by convection below the airstream. This can be seen in the heating by convection in Fig. 11b and c. The "DI-below" airstream descends slower than the "WCB-DI-above" airstream. In fact, the criterion of 400 hPa descent in two days to select DI trajectories proposed by Wernli (1997) and Raveh-Rubin (2017) would not detect all the trajectories in the airstream. However, the airstream serves well to illustrate the influence of convection on the descending airmass.

Until 29 January the "DI-below" airstream moves in an area of enhanced descent, below the southwestern part of the upper level trough, that later forms the PV streamer and stratospheric cutoff described in Sect. 3.1 (see the position of the trajectory relative to the tropopause in Fig. 10). Figure 12 shows a pseudo-sounding calculated from the model data at the location of the "DI-below" airstream at 18 UTC on 27 January (27°N, 52°W). The profile is representative for the first descent segment of the "DI-below" airstream in the troposphere. Below 600 hPa the profile is characterized by a moist and nearly

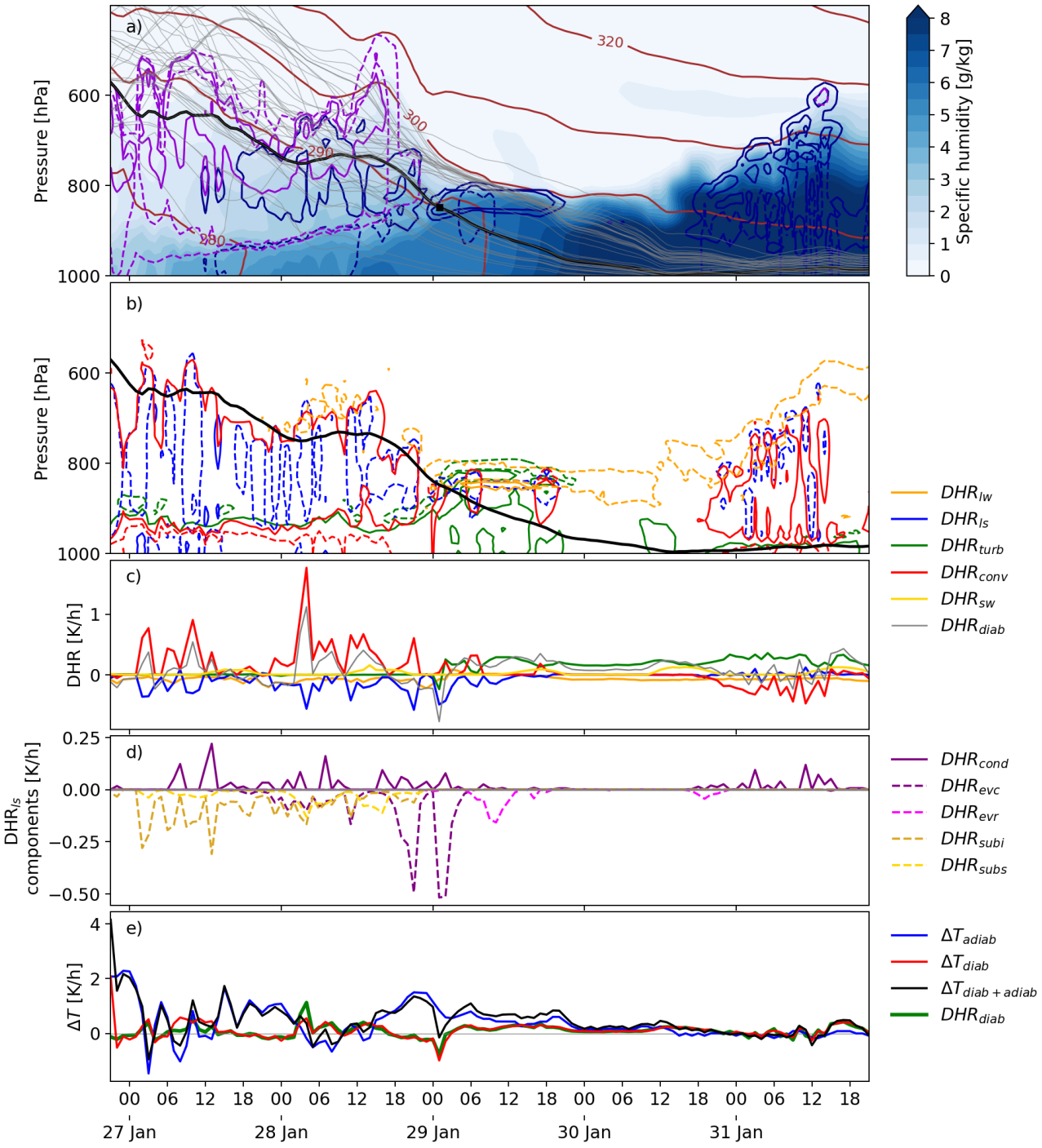


*Figure 11: a,b) Vertical cross sections along the one selected "DI-below" trajectory. a) The selected trajectory (black lines), other trajectories of the "DI-below" airstream (grey lines), specific humidity (shading), cloud and ice water content (blue and purple solid contours for 10 and* $50\,\mathrm{mg\,kg^{-1}}$*), rain and snow water content (blue and purple dashed contours for 1 and* $5\,\mathrm{mg\,kg^{-1}}$*), potential temperature [K] (brown contours). b) DHRs (solid contours for* $0.2\,\mathrm{K\,h^{-1}}$ *warming and dashed contours for* $-0.2\,\mathrm{K\,h^{-1}}$ *cooling) and the selected trajectory (black). c) DHRs at the trajectories' location. d)* $DHR_{ls}$*-components reaching absolute values bigger than* $0.01\,\mathrm{K\,h^{-1}}$*. e) Partitioning of the temperature tendencies as described in Sect. 2.5. The difference between* $\Delta T_{diab}$ *and* $DHR_{diab}$ *is the residual term. Note that the y-Axis in a) and b) only goes to 400 hPa (200 hPa in Fig. 9).*

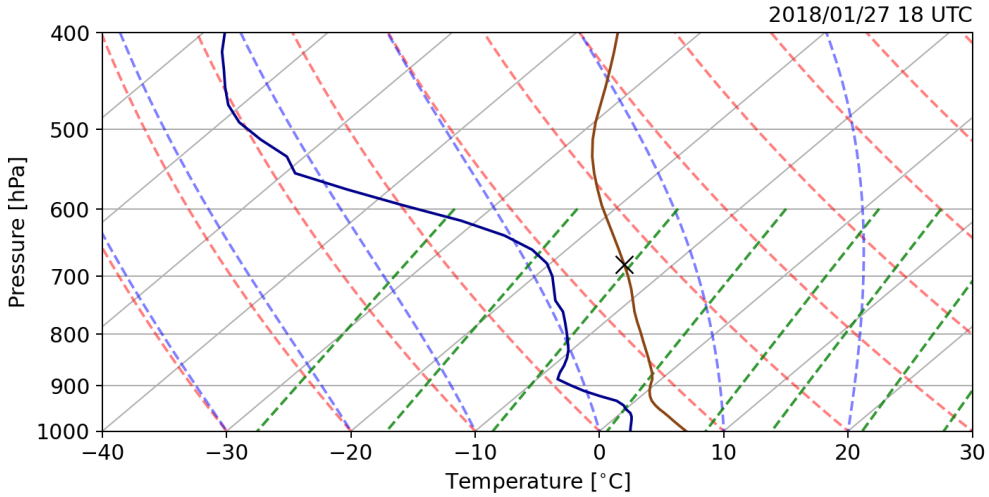


*Figure 12: Skew-T log-P diagram calculated from the IFS data at the horizontal position of the selected "DI-below" trajectory at 18 UTC on 27 January (27° N, 52° W). Temperature (brown) and dewpoint temperature (blue), with isobars (grey horizontal lines), isotherms (grey tilted lines), dry adiabates (orange dashed lines), moist adiabates (blue dashed lines) and lines of constant saturated specific humidity (green dashed lines). The cross indicates the temperature and height of the trajectory.*

adiabatic temperature profile. This is where convection is active, as can be seen in the heating due to convection in Fig. 11b. The layer above is dry and stably stratified. Most of the trajectories of the "DI-below" airstream move in this layer (see trajectories marked in grey in Fig. 11a). The one selected trajectory moves at the interface of the moist layer below and the dry stable layer above. Here, subgrid-scale convection injects moisture and heat into the dry DI airmass above (note areas of enhanced convective heating in Fig. 11b) and leads to notable cloud ice, snow and liquid water contents between 800 and 600 hPa (Fig. 11a).

Heating from the convection scheme dominates the diabatic temperature tendencies of the "DI-below" airstream between 27 January and 29 January (Fig. 11b). The airstream moves between altitudes of strong convective warming in the convective active region and higher altitudes, that are unaffected by convection. This leads to fluctuations in the strength of convective heating along the airstreams descent path, with rates between $0\,\mathrm{K\,h^{-1}}$ and $1.8\,\mathrm{K\,h^{-1}}$ (Fig. 11b,c). Periods of enhanced diabatic warming in the convective region likely cause the short ascent phases of the selected "DI-below" trajectory, that interrupt the general descent of the "DI-below" airstream at around 6 UTC on January 27 and 28 (Fig. 11a). Such ascent periods on time-scales of a few hours manifest in negative adiabatic heating rates, seen in Fig. 11e. When reaching above the convective region, longwave radiative cooling leads to a steady diabatic cooling of the airstream. This cooling might reinforce descent, until the airstream reaches again into a region of enhanced convective warming below. In the convective region, ice and snow sublimation, as well as evaporative cooling contribute to a diabatic cooling from the large-scale microphysics scheme, which partly offsets the convective warming (Fig. 11c).

In this segment the total temperature tendency is dominated by adiabatic temperature

changes (Fig. 11e). However, diabatic heating in the convective region and the diabatic cooling above feed back into vertical motion resulting in further adiabatic temperature modification. DI-airmasses at higher altitudes than the here selected trajectory are dryer and less affected by convection underneath (not shown).

**Descent segment in the boundary layer:** On 29 January the "DI-below" airstream penetrates into the boundary layer as described in detail in the next paragraph. The current paragraph focuses on the descent segment within the boundary layer. As described in the following, the DHRs in the boundary layer clearly differ from those observed above the boundary layer.
The airstream arrives in the boundary layer behind the cold front introduced in Sect. 3.1. From there the "DI-below" airstream travels with the trade winds southwestwards to Barbados (Fig. 10 between 29 January and the arrival of the airstream at the BCO). During this travel a thermal inversion builds above the airstream's path at the top of the mixed layer (not shown). Clouds form just below the inversion. These clouds can be seen in Fig. 11a between 29 January and 30 January. At first the airstream warms adiabatically and diabatically due to turbulent heat fluxes and convection (Fig. 11c between 29 January and 30 January). Evaporation of precipitation falling into the airstream cools the DI-airmass (Fig. 11d around 10 UTC on January 29). On 30 January the airstream is in a cloud-free environment. Here, convection and evaporation are not relevant and warming due to turbulence becomes dominant. At that time, warming due to turbulence is about three times stronger than longwave radiative cooling (Fig. 11c). The shortwave radiation shows a daily cycle. When it is maximal at local noon, it warms the airstream at a rate of $0.2\,\mathrm{K\,h^{-1}}$. Around 14 UTC on January 30, the selected trajectory passes trough the cold front into the warm region ahead of the front. This is indicated in Fig. 13a, where the trajectory passes from the area with low equivalent potential temperature behind the front into the warmer and moister air ahead. At 14 UTC the trajectory is in the region with the highest horizontal gradient of equivalent potential temperature (not shown). Thereafter, the thermal inversion at the top of the mixed layer disappears (not shown), turbulent warming and convection increase and the airstream slightly ascends (Fig. 11a,b and c). Clouds and precipitation affect the thermodynamic properties of the airstream on 31 January. Convection has a cooling effect on the lower troposphere and hence on the trajectory, presumably due to below cloud evaporation of rain (Fig. 11b and c). At the same time condensation from the large-scale microphysics scheme heats the airstream. Variability in the strength of the convective cooling results in fluctuations in the total temperature tendency, which on 31 January is dominated by diabatic warming from the turbulence scheme (Fig 11c and e).

**Penetration into the boundary layer:** Following a strong diabatic cooling at 01 UTC on 29 January, the trajectory descends trough a stable layer into the mixed boundary layer while increasing its humidity. This step is further analysed here, because the penetration into the boundary layer is an important time step to understand the interaction between the DI, the structure of the boundary layer and clouds often found at the top of the boundary layer. It is further interesting that the airstream penetrates into the boundary layer, although the boundary layer is often topped by a thermal inversion.

At 01 UTC the airstream is located in an extended region of enhanced descent to the southwest of the surface low pressure system (around 35°N, 40°W in Fig. 13a), which is coupled to the upper level PV cutoff described in Sect. 3.1. The cold front can be seen in Fig. 13a in the strong horizontal gradient of equivalent potential temperature. It is about 400 km to the south of the airstream. In the vertical cross section in Fig. 13b, the cold front can be seen around 25°N by the steep slope in the isentropes, which result in a strong horizontal temperature gradient. Below the trajectory, between 27°N and 29°N a slot of dry air reaches to the ground. At the horizontal position of the trajectory (28°N, 45°W), especially dry air reaches from the free troposphere to below 800 hPa. The selected "DI-below" trajectory is at the lower end of this descending dry air tongue at 848 hPa. In the pseudo-sounding in Fig. 14 it can be seen, that the trajectory is in a stable layer at the top of the mixed layer. At the altitude of the trajectory, the relative humidity sharply decreases with height, whereas the mixed layer below is characterized by nearly constant specific humidity and potential temperature.

At the location, where the trajectory penetrates through the stable layer at the top of the mixed layer (28°N, 45°W), subgrid-scale clouds contribute to the evaporative cooling of the airstream. This can be seen in the diabatic cooling due to evaporation in Fig. 11b. Resolved-scale clouds are further to the north and south (see regions of high relative

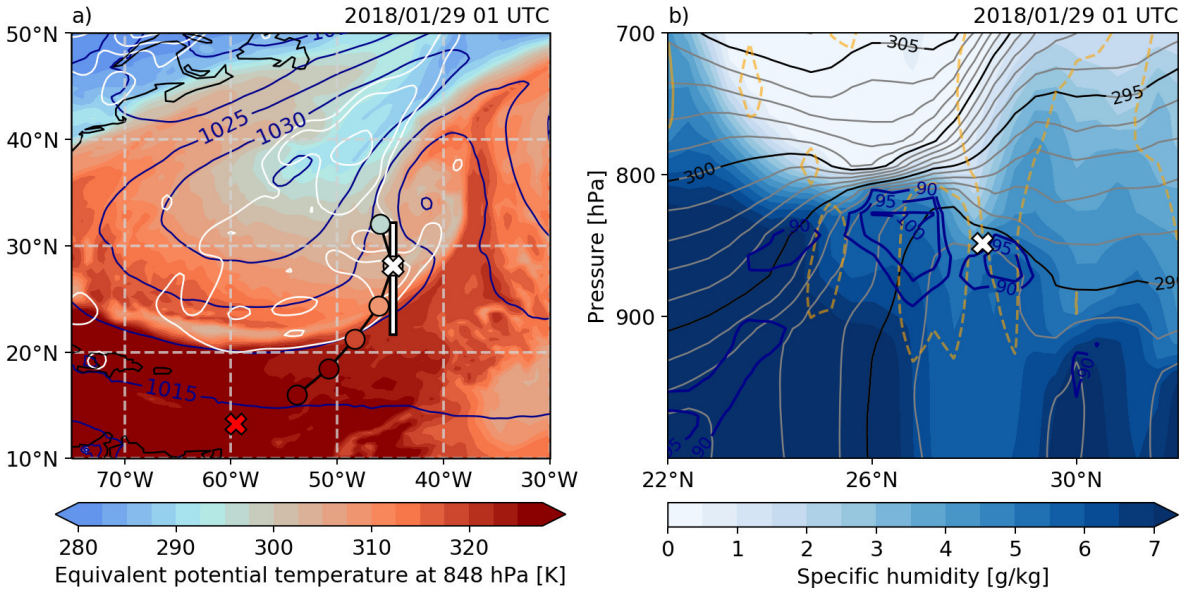


*Figure 13: Environment of the "DI-below" trajectory at 01 UTC on 29 January. a) Horizontal field at 848 hPa (the height of the selected trajectory): equivalent potential temperature (colors) and vertical wind $\omega$ (white contours for 0.1, 0.15 and $0.2\,\mathrm{Pa\,s^{-1}}$ descent, ascent is not shown) and sea level pressure [hPa] (blue contours). The white cross indicates the position of the trajectory at 01 UTC on 29 January and points show its position and equivalent potential temperature before and after in twelve hour intervals. The red cross indicates the position of Barbados (BCO). b) Cross section along the white line in panel a: specific humidity (shading), vertical wind $\omega$ (dashed orange lines for $0.2\,\mathrm{Pa\,s^{-1}}$ descent, ascent is not shown), potential temperature (black lines in 5 K intervals and grey lines in 1 K intervals) and relative humidity [%] (blue lines).*

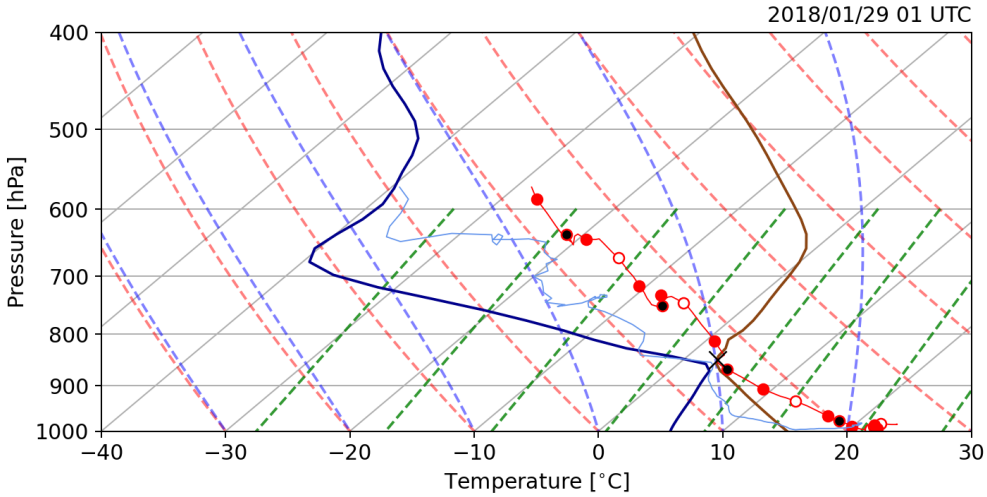


*Figure 14: Skew-T log-P diagram calculated from the IFS data at the position of the selected "DI-below" trajectory at 01 UTC on 29 January (28° N, 45° W). Temperature (brown line) and dewpoint temperature (darkblue line), with isobars (grey horizontal lines), isotherms (tilted grey lines), dry adiabates (orange dashed lines), moist adiabates (blue dashed lines) and lines of constant saturated specific humidity (green dashed lines). The temperature and dewpoint temperature along the trajectory are given in red and lightblue. Dots mark the trajectories temperature and pressure every six hours, where white filled dots mark the temperature at local noon. The black cross marks the temperature and height of the trajectory at 01 UTC on 29 January.*

humidity in Fig. 13b). Shortly before the airstream arrives at the location, where it penetrates into the boundary layer, the boundary layer is capped by a thermal inversion (see Fig. 15). Possibly the strongly descending motion in the DI environment leads to a local erosion of this inversion. At 01 UTC the inversion disappears, which enables the DI airstream to penetrate into the boundary layer. Higher up at around 700 hPa a new inversion builds 5 hours after the penetration (not shown).

The arrival of the airstream at the top of the boundary layer is accompanied by strong diabatic cooling from the evaporation of cloud droplets, turbulent mixing and longwave radiative cooling. The total diabatic cooling with a rate of $-0.8\,\mathrm{K\,h^{-1}}$ is large enough to offset the adiabatic warming (see Fig. 11c and e at 01 UTC on 29 January) and reinforce a further descent through the stable layer at the top of the boundary layer. At the same time the airstream moistens and reaches its maximal $\Delta q_{diab}$ of $1.2\,\mathrm{g\,(kg\,h)^{-1}}$ (Fig. 16).

For the selected trajectory, we found that its arrival at the boundary layer is marked by a strong diabatic cooling and a moistening of the airstream. At the same time the temperature inversion at the top of the boundary layer locally weakens. However, these findings are based on the analysis of only one selected trajectory. To find common features of the "DI-below" trajectories when penetrating into the boundary layer, we specify the time step of interest for each trajectory individually. We use the strong signal in $\Delta q_{diab}$ to identify the time step $t_{\Delta q,max}$, where a trajectory descending from the dry free atmosphere reaches a moist, sometimes cloudy layer often at the top of the boundary layer. It has to be noted, that some trajectories exhibit strong $\Delta q_{diab}$ at several time steps. To exclude

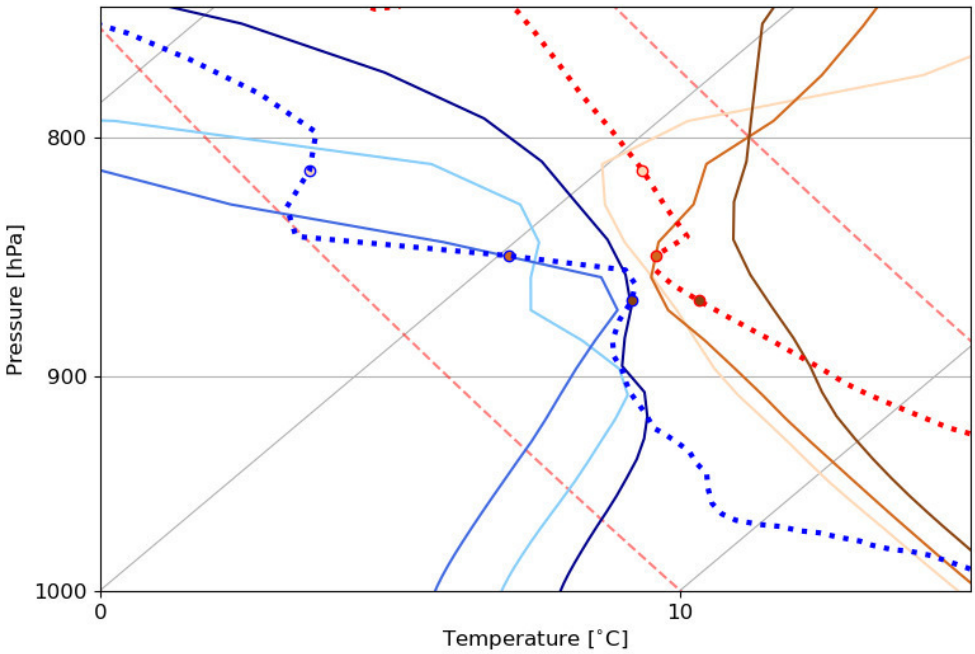


*Figure 15: Skew-T log-P diagram as in Fig. 14 at the position of the selected "DI-below" trajectory at 01 UTC on 29 January (28° N, 45° W), with profiles three hours before the arrival of the trajectory (temperature (darkbrown) and dewpoint temperature (darkblue)), at the arrival time of the trajectory (01 UTC) (temperature (medium brown) and dewpoint temperature (medium blue)) and three hours after the arrival of the trajectory (temperature (lightbrown) and dewpoint temperature (lightblue)). The temperature and dewpoint temperature along the trajectory are shown by red and blue dashed lines.*

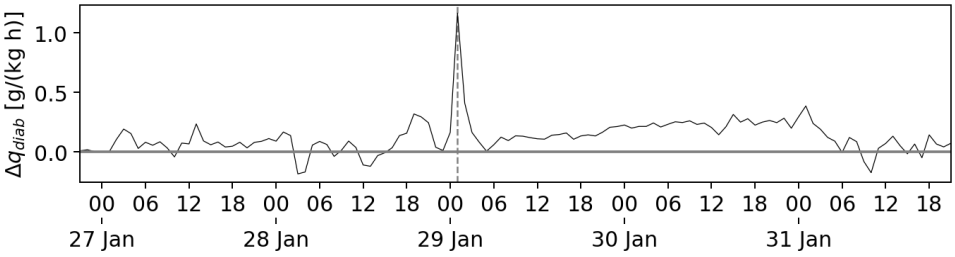


*Figure 16: $\Delta q_{diab}$ along the selected "DI-below" trajectory. The dashed line marks the maximum.*

humidity tendencies in the sub-cloud layer, we select $t_{\Delta q,max}$, individually at the time of maximal $\Delta q_{diab}$ along the trajectories path above 940 hPa. The average environment of the airstream at $t_{\Delta q,max}$ is shown in Fig. 17c and d. The composites are constructed as averaged vertical cross sections in north-south direction through the position of the 39 trajectories, roughly perpendicular to the direction of the DI trajectories. The composites are centred around $loc_{\Delta q,max}$, which is the trajectories' individual location at $t_{\Delta q,max}$. The "DI-below" airstream descends from a dry cold environment in the north to a warmer and more humid environment to the south, closer to the tropics. At $t_{\Delta q,max}$, a dry air tongue associated with the "DI-below" airstream, increases the vertical gradient in specific humidity at $loc_{\Delta q,max}$ (Fig. 17c). The connection of the dry air tongue with the "DI-below" airstream gets evident form their joint descent path to the south (note the displacement of the dry air tongue from Fig. 17a to c and e, along with the mean descent path of the airstream). The airstream is further linked to a region of amplified descent. At the selected time step, some trajectories encounter clouds below (see areas of enhanced relative humidity in Fig. 17).

Locally at $loc_{\Delta q,max}$ a temperature inversion is evident in the composites five hours before and at $t_{\Delta q,max}$. Five hours later $loc_{\Delta q,max}$ is in a vertically nearly isothermal layer. The erosion of the temperature inversion might be related to the strong descending motion in the DI environment, which is indicated by orange contours in Fig. 17.

The DHR at $t_{\Delta q,max}$ is shown in Fig. 18a. At that time all the 39 trajectories are diabatically cooled. The median $DHR_{diab}$ is $-0.8\,\mathrm{K\,h^{-1}}$. Longwave radiative cooling at cloud top and turbulent cooling are both important processes contributing to the total cooling. However, strong cooling rates are more frequently caused by longwave radiative cooling. In rare cases, both turbulence and longwave radiation cause a warming. Cloud microphysical processes, mostly evaporation, also generally cool, but at a smaller rate than the longwave radiative cooling. For trajectories reaching their maximal $\Delta q_{diab}$ during daytime, the cooling at the top of the mixed layer is partly offset by shortwave radiation. The effect of convection is overall small. As mentioned above, this strong diabatic cooling of the air parcel at cloud top, might be crucial for its further descent.

Attinger et al. (2019) analysed similar airstreams, which descend and penetrated behind a cold front into the boundary layer. Similar to the "DI-below" airstream, these airstreams cooled due to turbulence when arriving at the top of the boundary layer. In agreement with the "DI-below" airstream, turbulence warmed these airstreams once they arrived in the boundary layer. Attinger et al. (2019) further found strong DHRs from microphysical processes in the vicinity of the cold front. This is not observed for the "DI-below" airstream in this study.

Turbulent mixing of moist air into the DI airmass causes the strong $\Delta q_{diab}$, used to identify the airstreams arrival time at the boundary layer top (see Fig. 18b). Convection also plays an important role in increasing the air parcels' humidity. Similar to the diabatic modification of the air parcel, the effect of the cloud microphysics scheme is of minor importance for the $\Delta q_{diab}$ at $t_{\Delta q,max}$.

When considering DHRs at $t_{\Delta q,max}$, dynamical effects associated with the large-scale weather situation must be considered. Similar to the selected trajectory described in the first part of this section, all the trajectories reach their maximal $\Delta q_{diab}$ in close vicinity of the cold front (Fig. 19). While three trajectories reach their maximal $\Delta q_{diab}$ in the extra-

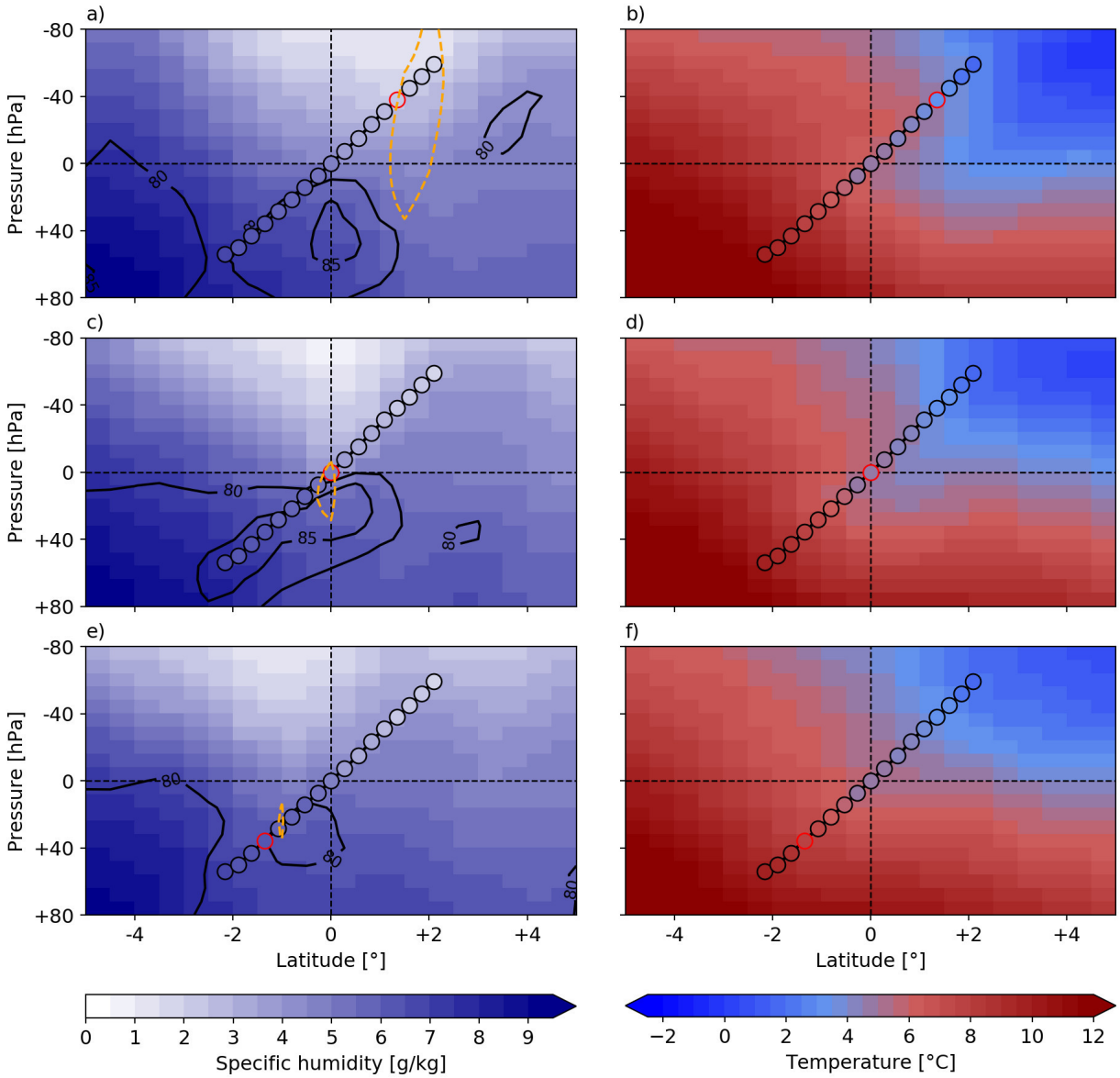


*Figure 17: Average environment at $loc_{\Delta q,max}$ (the individual location where $\Delta q_{diab}$ reaches its maximum along a trajectory, above 940 hPa): For every trajectory a north-south cross section is taken at $loc_{\Delta q,max}$. The composites show the average of these cross sections, centred around the $loc_{\Delta q,max}$ a,b) five hours before $t_{\Delta q,max}$ (the individual time of the maximal $\Delta q_{diab}$) c,d) at $t_{\Delta q,max}$ and e,f) five hours after $t_{\Delta q,max}$. a,c,e) Specific humidity (shading), relative humidity [%] (contours) and vertical wind $\omega$ (orange contours for descent $> 0.2\,\mathrm{Pa\,s^{-1}}$). b,d,f) Temperature (shading). Dots indicate the average path from north to south of the trajectories, by indicating the position, a) specific humidity and b) temperature hourly. The trajectories latitude and pressure at the time of the composite is indicated by the red dot. Note that the longitude of the cross section is fixed to $loc_{\Delta q,max}$ and does not follow the trajectories.*

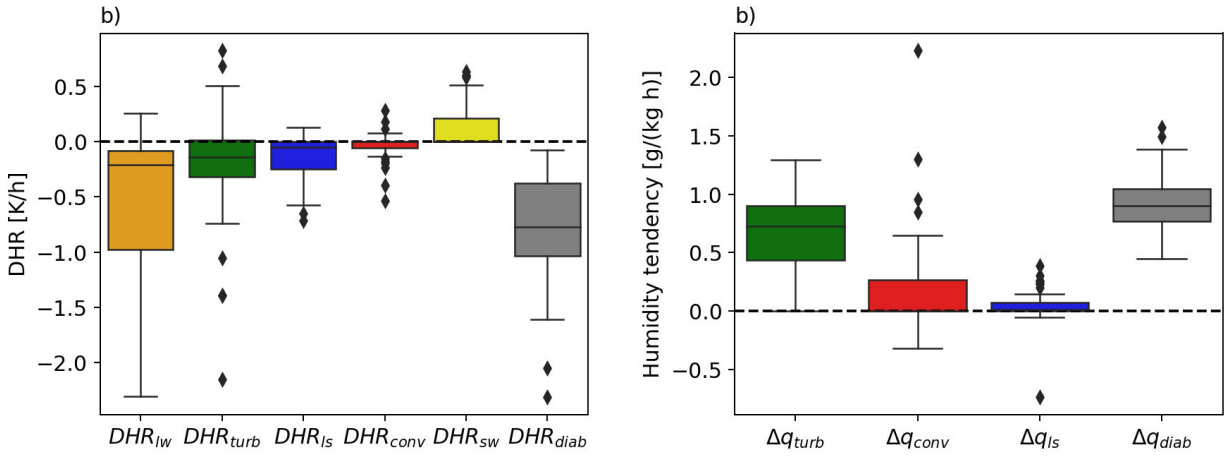


*Figure 18: Processes at $t_{\Delta q,max}$ (the time step of the maximal $\Delta q_{diab}$ above 940 hPa along the trajectory) for the trajectories of the "DI-below" airstream. a) DHR and b) $\Delta q_{diab}$ split into the different parametrized processes. Whiskers show 1.5 × IQR.*

tropics northwards of 30°N, the other 36 trajectories are located between 20°N and 30°N at their respective $t_{\Delta q,max}$. Most of the trajectories are a few hundred kilometres behind the cold front, and pass trough it within the following day. Some trajectories are already roughly at the latitude of the cold front, when reaching their strongest $\Delta q_{diab}$ (Fig. 19c). The enhanced subsidence at that time step, might therefore result from ageostrophic circulations associated with the front. For further studies a clear definition of the boundary layer height would help to assess how the boundary layer is affected by the front and to clearly distinct diabatic processes happening at the front from processes happening at the top of the boundary layer.

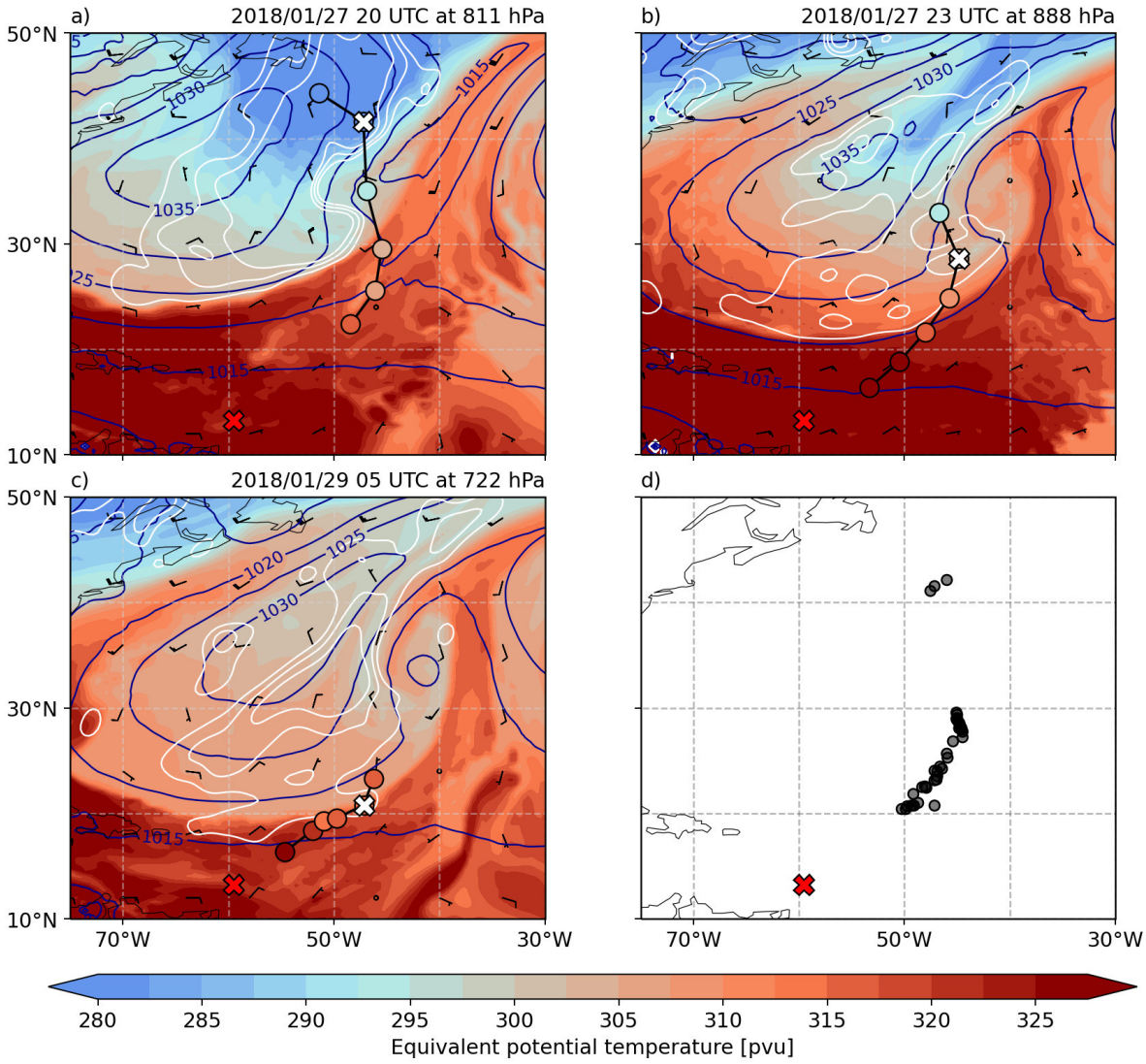


*Figure 19: Horizontal position of "DI-below" trajectories at their individual $t_{\Delta q,max}$ (the time step of the maximal $\Delta q_{diab}$ above 940 hPa along the trajectory). a-c) Field for individual trajectories at their respective pressure level, indicated in the title: equivalent potential temperature (colors), wind barbs (black) and vertical wind $\omega$ (white contours for 0.1, 0.15 and $0.2\,\mathrm{Pa\,s^{-1}}$ descent, ascent is not shown) and sea level pressure [hPa] (blue contours). The white cross indicates the position of the trajectories at $t_{\Delta q,max}$ and points show their position and equivalent potential temperature before and after in twelve hour intervals. d) Horizontal position of all trajectories at their $t_{\Delta q,max}$. The red cross indicates the position of Barbados (BCO).*

## 3.4 Typical trade wind flow airstreams

In this section, two airstreams are introduced, that arrive at the BCO before the influence of the PV cutoff on the trajectories becomes evident: 1.) A tropical airstream, that travels from the east to Barbados within the cloud layer. It belongs to the darkblue category in Fig. 7a. In the following it will be referred to as the "Trop" airstream. 2.) An airstream belonging to the turquoise category in Fig. 7a, which origins in the subtropics and moves within the sub-cloud layer. This airstream will be referred to as the "SubTrop" airstream.

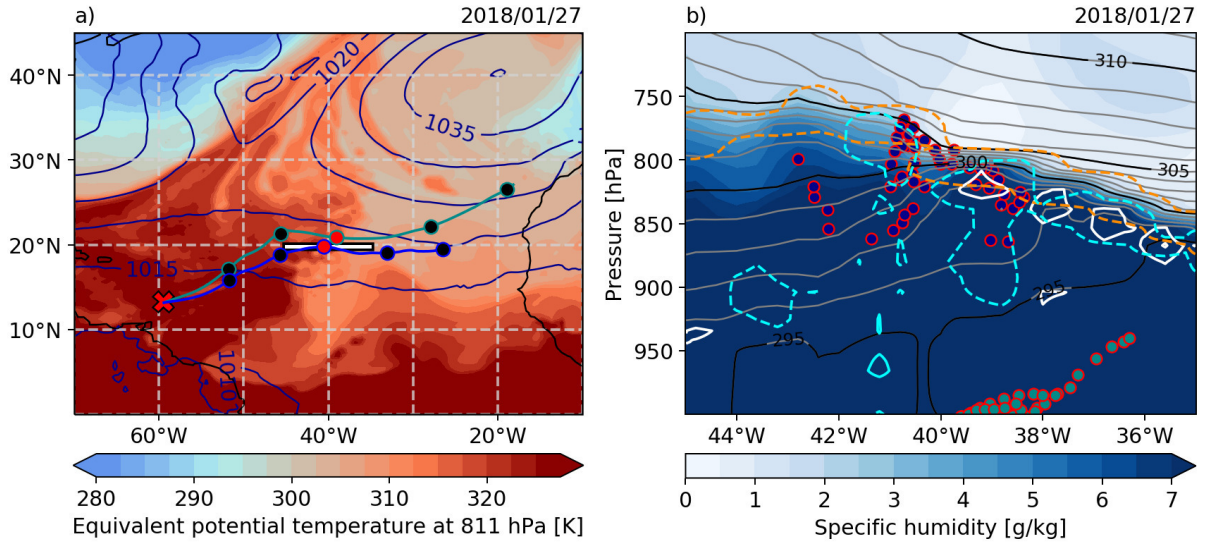


*Figure 20: a) Path of the "Trop" (blue line) and "SupTrop" (turquoise line) airstream. The median locations of the trajectories are indicated by dots every day at 00 UTC, with the red dot giving the position on 27 January. Equivalent potential temperature (colors) at 00 UTC on 27 January at 811 hPa (the median pressure of the "Trop" airstream at that time) and sea level pressure [hPa] (blue contours). The red cross indicates the location of Barbados (BCO). b) Cross section along the white line in panel a: specific humidity (shading), relative humidity (white contours indicate regions of 90%) , $DHR_{lw}$ (orange) and $DHR_{ls}$ (blue) (dashed contours mark cooling of $-0.2\,\mathrm{K\,h^{-1}}$.), potential temperature (black lines in 5 K intervals and grey lines in 1 K intervals) and the pressure and longitude of the trajectories belonging to the "Trop" (blue dots) and "SubTrop" (turquise dots) airstream.*

**"Trop" airstream:** The "Trop" airstream starts on 25 January north of Kap Verde at 820 hPa, above the cloud layer (Fig. 20a and 21a). Here, longwave radiative cooling dominates the diabatic temperature tendency (Fig. 21c). The shortwave radiative heating shows a daily cycle. At local noon, when shortwave radiation is maximal, the shortwave radiative warming offsets the cooling. While the airstream moves on a constant pressure level to the east, its environment warms and moistens. This can be seen in Fig. 20a, where the low-level equivalent potential temperature increases from the east towards the west Atlantic trade wind region. This pattern holds qualitatively over the trajectories' five day period (not shown). Convection below the airstream strengthens from 26 January

to 27 January (note the increased area of convective warming with rates above $0.2\,\mathrm{K\,h^{-1}}$ in Fig. 21b). At the same time the height of the mixed layer increases, this can be seen in the increasing height of the sharp specific humidity gradient in Fig. 21a, that marks the top of the mixed layer. Between 26 and 27 January clouds reach the height of the airstream (Fig. 21a). At cloud top the airstream is cooled diabatically, similar to the DI airstreams, by longwave radiation and evaporation of cloud droplets (Fig. 11c).

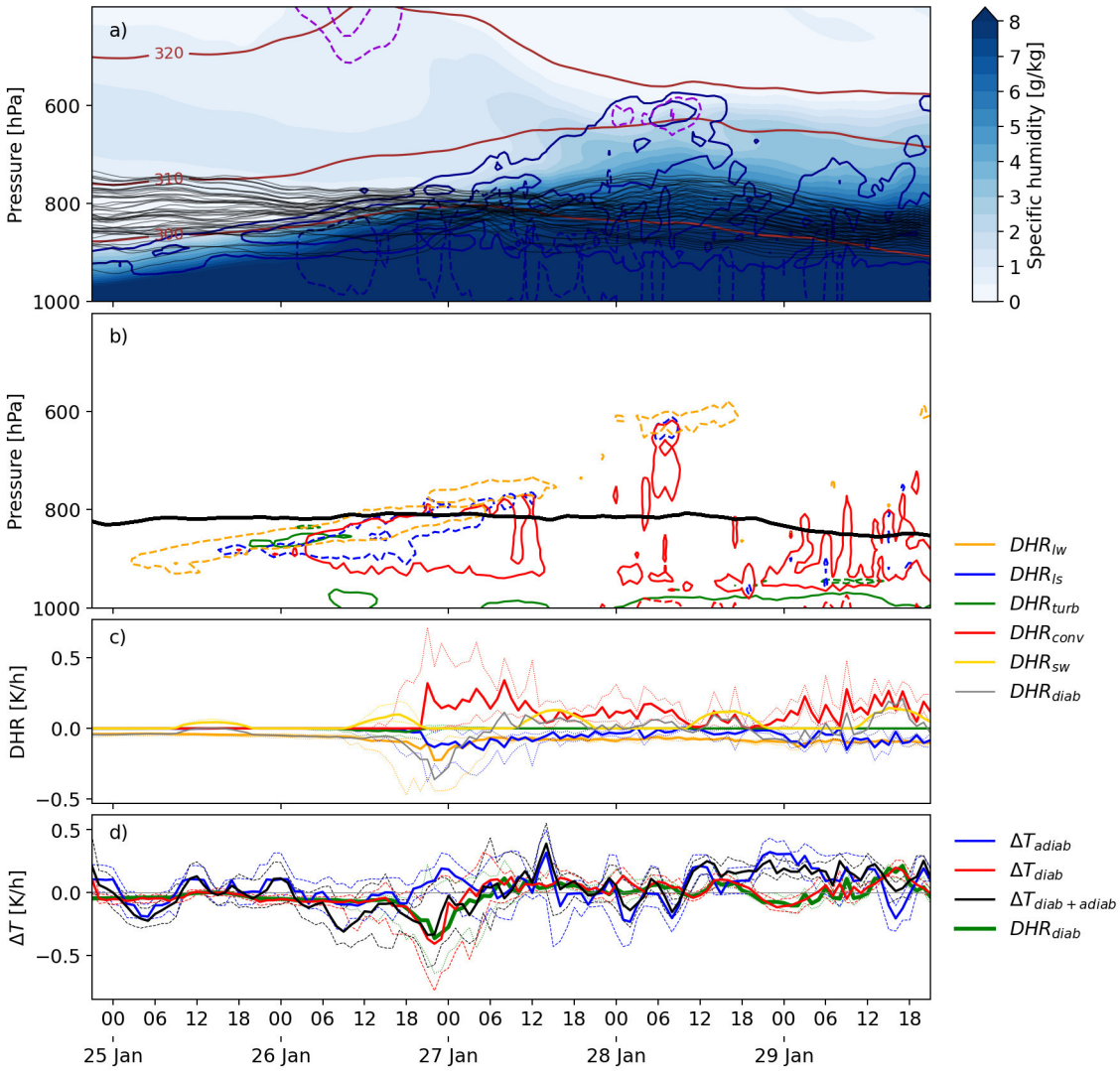


*Figure 21: a,b) Mean vertical cross sections along the "Trop" airstream. a) Trajectories (black lines), specific humidity (shading), cloud and ice water content (blue and purple solid contours for 10 and $50\,\mathrm{mg\,kg^{-1}}$), rain and snow water content (blue and purple dashed contours for 1 and $5\,\mathrm{mg\,kg^{-1}}$) and potential temperature [K] (brown contours). b) DHRs (solid contours for $0.2\,\mathrm{K\,h^{-1}}$ warming and dashed contours for $-0.2\,\mathrm{K\,h^{-1}}$ cooling) and the median of the trajectories' position (black). c) DHRs at the airstreams' location, where the cooling from $DHR_{ls}$ is nearly exclusively due to $DHR_{evap}$. d) Partitioning of the temperature tendencies as described in Sect. 2.5. The difference between $\Delta T_{diab}$ and $DHR_{diab}$ is the residual term. Solid lines in c and d and mark the median and dashed lines the 0.25 and 0.75 quantiles.*

Simultaneously a slight descent, likely caused by the diabatic cooling, can be seen in the positive adiabatic temperature tendency (Fig. 21d at 00 UTC on 27 January). However, the "Trop" trajectory shows generally small vertical displacement and the diabatic cooling dominates over the adiabatic warming when entering into the boundary layer. Strong convective warming in the mid and lower part of the convective clouds warms some of the lower "Trop" trajectories. During the further path of the airstream in the convective clouds, convective warming and shortwave warming mostly dominate over diabatic cooling from longwave radiation and and evaporation (Fig. 21c).

**"SubTrop" airstream:** This subtropical airstream starts above the Canaries at 1010 hPa close to the sea surface (see Fig. 20a and 22a). It travels to Barbados on a nearly constant pressure level in the sub-cloud layer. Adiabatic temperature tendencies are hence small (Fig. 22d). Turbulence and shortwave radiation during daytime add to a mostly positive diabatic temperature tendency (Fig. 22c). Particularly below areas with deep convection, the convective scheme cools the airstream, possibly due to evaporation of convective precipitation. Longwave radiation accounts for a cooling of about $-0.1\,\mathrm{K\,h^{-1}}$. The large-scale micro physics scheme has only minor impacts on the "SubTrop" airstream.

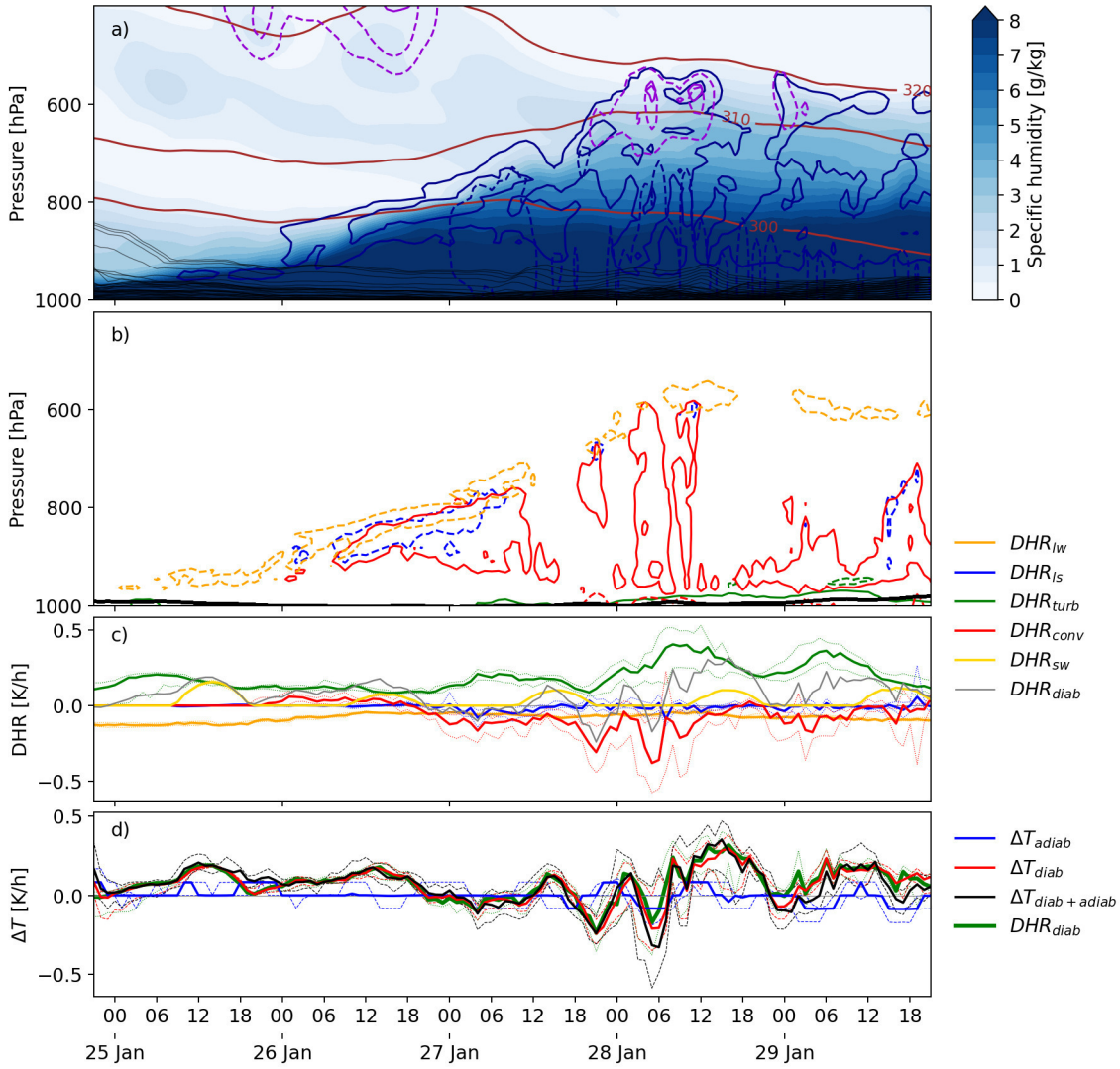


*Figure 22: a,b) Mean vertical cross sections along the "SubTrop" airstream. a) Trajectories (black lines), specific humidity (shading), cloud and ice water content (blue and purple solid contours for 10 and* $50\,\mathrm{mg\,kg^{-1}}$*), rain and snow water content (blue and purple dashed contours for 1 and* $5\,\mathrm{mg\,kg^{-1}}$*) and potential temperature [K] (brown contours). b) DHRs (solid contours for* $0.2\,\mathrm{K\,h^{-1}}$ *warming and dashed contours for* $-0.2\,\mathrm{K\,h^{-1}}$ *cooling) and the median of the trajectories' position (black). c) DHRs at the airstreams' location. d) Partitioning of the temperature tendencies as described in Sect. 2.5. The difference between* $\Delta T_{diab}$ *and* $DHR_{diab}$ *is the residual term. Solid lines in c and d and mark the median and dashed lines the 0.25 and 0.75 quantiles.*

## 3.5 Comparison of the thermodynamic history of dry intrusion airstreams and typical trade airstreams

In this section the thermodynamic history of the two DI airstreams, that are described in Sect. 3.3, and the typical trade airstreams, introduced in Sect. 3.4, are discussed and compared. Figure 23 shows their Lagrangian evolution in a phase space of temperature (T) and potential temperature ($\Theta$). This allows to summarize the adiabatic and diabatic temperature changes of the four airstreams (Bieli et al., 2015; Aemisegger et al., 2020). In the figure adiabatic temperature changes appear as changes in T, while $\Theta$ remains constant (horizontal movements in Fig. 23). Diabatic temperature tendencies lead to a $\Theta$ modification (i.e. a deviation from horizontal movements in Fig. 23).

The three segments of the "WCB-DI-above" airstream, described in Sect. 3.3.1, are clearly distinguishable in Fig. 23a. The airstreams' ascent as a WCB between 27 and 29 January is followed by the DI-descent and the arrival at cloud top on 31 January. During the ascent, the "WCB-DI-above" airstream shows a strong adiabatic cooling of 60 K. The total diabatic warming between 27 and 29 January of 20 K, is typical for WCBs (Madonna et al., 2014). The airstream ends its ascent on 29 January with a $\Theta$ of 321 K. This is in the expected range for WCBs during winter, which typically reach $\Theta$ values between 313 and 321 K (Madonna et al., 2014). The ascent is further accompanied by a decrease in specific humidity to nearly $0\,\mathrm{g\,kg^{-1}}$. Typically, condensation in the early ascent phase and depositional grow of ice in the later ascent phase lead to the decrease in the air parcels' water vapour content (Madonna et al., 2014). Thus, the airstream is very dry when it starts descending as a DI at 300 hPa on 29 January. WCBs normally descend slowly or remain in the jet stream region for a few days after a strong two day ascent, in this respect the "WCB-DI-above" descent is particularly strong. Between 29 January and 31 January specific humidity stays low, while the airstream descends from the upper troposphere. The descent is nearly adiabatic, with a T increase of 50 K. The diabatic cooling of -3.6 K in two days is comparable to values found by Raveh-Rubin (2017). When arriving at cloud top, the airstream increases its humidity. This increase is dominated by a strong convective moistening at 11 UTC (not shown). At the same time, diabatic cooling is intensified.
The "DI-below" airstream starts its descend around 500 hPa, 200 hPa lower than the "WCB-DI-above" airstream. Similar to the "WCB-DI-above" airstream its specific humidity is low during the first descent day. Air parcels of the "DI-below" airstream start to take up moisture on 28 January. When the airstream reaches the top of the boundary layer on 29 January, specific humidity is significantly higher than in the "WCB-DI-above" airstream. The "DI-below" airstream descends more slowly than the "WCB-DI-above" airstream and its adiabatic warming of 50 K between 27 January and 29 January is weaker than the 60 K warming of the "WCB-DI-above" airstream during its respective descent (between 29 January and 31 January). The "DI-below" airstream starts its descent with a $\Theta$ of 297 K. This is 23 K less than the $\Theta$ of the "WCB-DI-above" airstream when starting its descent. During the major part of the descent, the diabatic cooling of the "DI-below" airstream is negligible. On 29 January it arrives at the top of the boundary layer with low $\Theta$ values compared to the "WCB-DI-above" airstream. At the top of the boundary layer the airstream takes up humidity and diabatically cools, similar to the "WCB-DI-

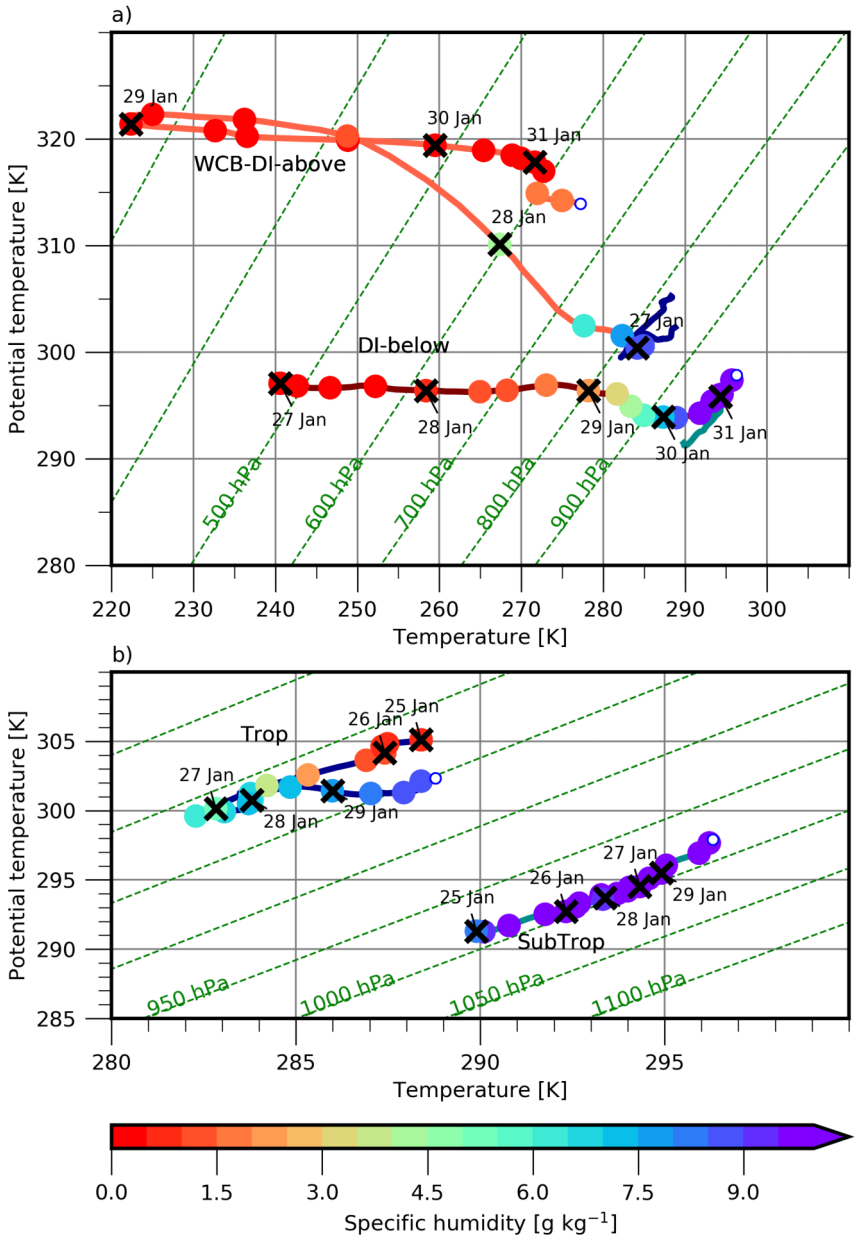


*Figure 23: Thermodynamic Θ-T diagram summarizing the Lagrangian history of a) the DI airstreams: "WCB-DI-above" (orange line) and "DI-below" (brown line) and b) the trade airstreams "Trop" (blue line) and "SubTrop" (turquoise line). Median values are shown every 6 hours by points coloured according to the airstreams specific humidity. The time is given at 00 UTC. The arrival conditions above Barbados are indicated by white dots. The slanted green lines show isobars, the horizontal lines isentropes and the vertical lines isotherms. To directly compare the Trade airstreams to the DI airstreams, their path in the Θ-T phase space is additionally given in panel a by the blue and turquoise line.*

above" airstream. The "DI-below" airstream further penetrates into the boundary layer, where its specific humidity increases to $9\,\mathrm{g\,kg^{-1}}$ and the airstream is diabatically warmed. Whether the "WCB-DI-above" airstream actually also descends more deeply into the boundary layer is not clear from the calculated trajectories, which end in Barbados at cloud top. To asses this question, it would be interesting to calculate forward trajectories from Barbados.

Note that the median of the trajectories belonging to the "DI-below" airstream are used in Fig. 23. This is different in Fig. 11, where only one trajectory of the "DI-below" airstream is selected. For this selected trajectory $\Theta$ shows pronounced fluctuations during the descent between 27 January and 29 January (not shown). Such fluctuations on short-time scales are not seen in the median in Fig. 23. This is because the timing of enhanced warming and cooling respectively differ between the individual trajectories. The selected "DI-below" trajectory is one of the lower trajectories in the airstream, as seen in Fig. 11a. Therefore, it interacts more with the convective region below (see Sect. 3.3.2). This is why the selected trajectory increases its humidity more rapidly in the first two days than the median of the airstream (not shown).

The "Trop" airstream shows nearly no horizontal displacement and moves between 800 and 850 hPa (Fig. 23b). Similar to the two DI-airstreams it starts with low specific humidity on 25 January. While the "Trop" airstream moves into the clouds on 26 January, the specific humidity strongly increases. The diabatic cooling of 5 K on this day is similar to the cooling of the DI-airstreams, when reaching the boundary layer. Unlike the "DI-below airstream, no strong descent follows this cooling. While remaining at 820 hPa, the airstream diabatically warms on 28 January and further moistens.

The "SubTrop" airstream starts with a high specific humidity in the boundary layer. During its five day travel from the east to the west Atlantic, the airstream stays moist and close to the sea surface. Its temperature changes with the increasing sea surface temperature along its path (not shown). In the five days of travel over the subtropical and tropical North Atlantic the airstream warms by 6 K.

To summarize this section: The trade airstreams move mostly on constant pressure levels and display only small adiabatic temperature changes. In contrast the DI airstreams exhibit strong vertical motion, that lead to substantial temperature tendencies. The largest diabatic cooling and the strongest moistening is due to the interaction of the air parcels with cloud tops.

# 4 Conclusions

Dry Intrusions (DI) play an important role in shaping the synoptic time-scale variability of the tropical low-level cloud cover. When the dry DI-air reaches into the low-levels, diabatic processes happening along it can influence boundary layer properties and thereby affect low-level clouds. With the global IFS model simulation from the ECMWF we investigate diabatic processes along DI air parcels descending from the extratropics into the western North Atlantic trade wind region. To identify DI airstreams, we calculated hourly backward trajectories form Barbados (BCO) for the isoTrade period from 25 January to 6 February 2018. Two DI airstreams are selected for detailed case studies based on their vertical motion: 1) An airstream, that ascends in the extratropics as a warm conveyor belt (WCB) and reaches 300 hPa before the rapid DI-descent into the trade wind region, where it arrives at the top of clouds. This airstream is referred to as "WCB-DI-above" airstream. 2) An airstream, that starts its descent around 500 hPa in the extratropics. After two days it penetrates behind a cold front into the subtropical boundary layer. This airstream is referred to as "DI-below" airstream. The two DI airstreams are compared to two typical trade wind airstreams: 1) A Tropical airstream, that moves within the cloud layer from the east to the west Atlantic. 2) An airstream that starts in the subtropical east Atlantic and moves close to the sea surface to Barbados. This airstream is referred to as the "SubTrop" airstream. Based on these four airstreams our conclusion with respect to the questions raised in Sect. 1 are as follows:

1. The DI event relates to an upper level PV cutoff over the central Atlantic, that coupled to a surface cyclone. The cutoff formed during an anticyclonic Rossby wave breaking event between 25 January and 29 January 2018. The two DI airstreams descend to the west of the cutoff in an extended region of enhanced descent, that is induced by the positive PV anomaly. The cyclonic wind field steered the DI airstreams southwards to Barbados. This relation between the anticyclonic Rossby wave breaking and the DI event is established by Aemisegger et al. (2020).

2. The path of the DI airstreams can be split into segments shaped by distinct diabatic processes. The strong ascent of the "WCB-DI-above" airstream is accompanied by a strong drying and diabatic warming from the large-scale microphysics and convection scheme, as typical for WCBs (Joos and Wernli, 2012; Madonna et al., 2014). During the descent, the "WCB-DI-above" airstream diabatically cools due to longwave radiation, which is partly offset by solar radiation. The total diabatic cooling of the "WCB-DI-above" airstream of -3.6 K in two descent days is comparable to values found by Raveh-Rubin (2017). When arriving at cloud top, the longwave radiative cooling is enhanced and at the same time evaporation of cloud droplets increases the cooling.

   The "DI-below" airstream starts at a lower altitude than the "WCB-DI-above" airstream. Its descent of about 300 hPa in two days, is slower than DIs analysed by Raveh-Rubin (2017). In the first descent segment convection heats the "DI-below" airstream, simultaneously evaporation cools. As for the "WCB-DI-above" airstream, diabatic cooling mostly due to longwave radiation is pronounced at cloud top. In the boundary layer the airstream diabatically warms due to turbulent processes.

Close to the sea surface the diabatic warming of the "DI-below" airstream is similar to the warming of the "SubTrop" airstream.

3. The penetration of the "DI-below" airstream into the boundary layer is an important time step to understand the interaction of the DI airmass with clouds, that are often found at the top of the boundary layer. We found an enhanced moistening and diabatic cooling of the DI airmass on top of the boundary layer. With the DI airstream dry air is transported to the top of the boundary layer, which locally increases the vertical humidity gradient. The strong cooling combined with a locally decreased stability at the top of the boundary layer enables the "DI-below" airstream to penetrate into the boundary.

4. Compared to the two typical trade wind airstreams that travel from the east over the Atlantic on a constant pressure level, the selected DI airstreams are special regarding their vertical motion associated with strong adiabatic temperature tendencies. In contrast to the trade-airstreams, the "DI-below" airstream vertically moves trough the different layers, and penetrates due to large-scale areas of descending motion into the boundary layer, where it further descends. Diabatic heating rates at the top of the boundary layer are similar for the typical trade wind airstreams and the DI airstreams.

Care must be taken, when interpreting the trajectories penetration into the boundary layer. Wind gradients close to the cold front and the boundary layer cause turbulence that affect the wind field. This can lead to uncertainties in the resolved wind and errors in the trajectory calculation (Spreitzer et al., 2019). Nevertheless, we found that the 39 analysed "DI-below" trajectories entered the boundary layer within an extended region of subsidence. The coherent penetration and and the large-scale signal in the vertical winds gives confidence in the physical entering of the DI airstream into the boundary layer. Calculating forward and backward trajectories in the region around the identified locations, where DI airmasses arrive on top of the boundary layer, could help assessing the coherence of the airstreams' movements and would allow to follow the fate of the boundary layer entering DI airstream. Whether the ageostropic circulation behind the cold front plays an important rule in facilitating the penetration of the DI airmass into the boundary layer could not be assessed in this case study. It would be insightful to calculate forward trajectories from Barbados, to find out, if the "WCB-DI-above" airstream also descends more deeply into the boundary layer ahead of the front. For further studies, a clear definition of the boundary layer height and the position of the cold front would help to assess how the boundary layer is affected by the front and to better distinguish diabatic processes related to the cold front from processes happening at the top of the boundary layer.

The magnitude of the observed diabatic heating rates (DHR) strongly depends on the selection of trajectories. Especially diabatic warming due to convection can vary strongly between a few grid cells. However, trajectories of the selected airstreams show consistency in terms of which diabatic process dominate in each segment of their path. Furthermore, uncertainties arise from using the instantaneous hourly DHR output of the IFS compared with the total temperature change of the air parcels (see Sect. 2.5). However, apart from a few time steps mostly relating to strong convective warming, the residual is small compared to the total diabatic heating rate. This is also the case for the strong diabatic

cooling at cloud top. As DHRs strongly depend on the parametrization of the model, it would be interesting to evaluate DHRs in other models.

This detailed case study of DI airmasses penetrating into the subtropical boundary layer and how they are influenced by parametrized diabatic processes in the model illustrates how DI modify their thermodynamic properties in the environment of the low-level clouds. A better physical understanding of the coupling between diabatic and adiabatic processes and of the role of clouds in this coupling is important to overcome uncertainties in climate models related to the cloud radiative feedback (Bony and Stevens, 2012). Further insights could be gained by investigating how the diabatic cooling of DI airmasses at the top of the boundary layer and the following descent of the DI airmass depend on and impact the cloud cover below. To get a more robust signal regarding which diabatic processes dominate and how they depend on boundary layer properties more cases should be analysed.

**Acknowledgement:** Throughout my master thesis I received a lot of help and support from many sides. I thank my supervisors Leonie Villiger, Dr. Franziska Aemisegger and Dr. Maxi Boettcher for all the inspiring discussions. I am grateful for their enthusiasm and useful feedback. I especially appreciate how I was integrated into the research group. I would also like to thank Prof. Dr. Heini Wernli and the whole IAC for giving me an insight into their research. A special thank goes to my study colleges for helpful tips, valuable input and motivating breaks. Finally I would like to thank my family and flatmates for their support.

# References


Aemisegger, F., Vogel, R., Graf, P., Dahinden, F., Bony, S., Stevens, B., and Wernli, H. (2020). How rossby wave breaking can modulate the trade wind water cycle above the tropical North Atlantic: A stable water isotope perspective. *in prep. for WCD*. doi: 10.5194/wcd-2020-51

Attinger, R., Spreitzer, E., Boettcher, M., Forbes, R., Wernli, H., and Joos, H. (2019). Quantifying the role of individual diabatic processes for the formation of PV anomalies in a North Pacific cyclone. *Q. J. R. Meteorol. Soc.*, *145*(723), 2454–2476. doi: 10.1002/qj.3573

Bieli, M., Pfahl, S., and Wernli, H. (2015). A Lagrangian investigation of hot and cold temperature extremes in Europe. *Q. J. R. Meteorol. Soc.*, *141*(686), 98–108. doi: 10.1002/qj.2339

Bony, S., and Dufresne, J.-L. (2005). Marine boundary layer clouds at the heart of tropical cloud feedback uncertainties in climate models. *Geophys. Res. Lett*, *32*(20). doi: 10.1029/2005GL023851

Bony, S., and Stevens, B. (2012). Clouds, circulation and climate sensitivity: How the interactions between clouds, greenhouse gases and aerosols affect temperature. *White Paper on WCRP Grand Challenge*.

Bony, S., Stevens, B., Ament, F., Bigorre, S., Chazette, P., Crewell, S., et al. (2017). EUREC $^4$A: A field campaign to elucidate the couplings between clouds, convection and circulation. *Surv. Geophys.*, *38*(6), 1529–1568. doi: 10.1007/s10712-017-9428-0

Bony, S., Stevens, B., Frierson, D. M., Jakob, C., Kageyama, M., Pincus, R., et al. (2015). Clouds, circulation and climate sensitivity. *Nat. Geosci.*, *8*(4), 261–268. doi: 10.1038/NGEO2398

Browning, K. (1997). The dry intrusion perspective of extra-tropical cyclone development. *Meteorol. Appl.*, *4*(4), 317–324. doi: 10.1017/S1350482797000613

Catto, J. L., and Raveh-Rubin, S. (2019). Climatology and dynamics of the link between dry intrusions and cold fronts during winter. part I: global climatology. *Clim. Dyn*, *53*(3), 1873–1892. doi: 10.1007/s00382-019-04745-w

Cau, P., Methven, J., and Hoskins, B. (2007). Origins of dry air in the tropics and subtropics. *J. Clim.*, *20*(12), 2745–2759. doi: 10.1175/JCLI4176.1

Hermann, M., Papritz, L., and Wernli, H. (2020). A Lagrangian analysis of the dynamical and thermodynamic drivers of Greenland melt events during 1979–2017. *Weather Clim. Dyn.*, 1–32. doi: 10.5194/wcd-1-497-2020

IFS documentation CY43R1 - part IV: Physical processes. (2016). In *IFS documentation CY43R1.* ECMWF. Retrieved from `https://www.ecmwf.int/node/17117` doi: 10.21957/sqvo5yxja

Joos, H., and Wernli, H. (2012). Influence of microphysical processes on the potential vorticity development in a warm conveyor belt: a case-study with the limited-area model COSMO. *Q. J. R. Meteorol. Soc.*, *138*(663), 407–418.

Madonna, E., Wernli, H., Joos, H., and Martius, O. (2014). Warm conveyor belts in the ERA-Interim dataset (1979–2010). part I: Climatology and potential vorticity evolution. *J. Clim.*, *27*(1), 3–26. doi: 10.1175/JCLI-D-12-00720.1

Medeiros, B., and Nuijens, L. (2016). Clouds at Barbados are representative of clouds across the trade wind regions in observations and climate models. *PNAS*, *113*(22), E3062–E3070. doi: 10.1073/pnas.1521494113

Nuijens, L., Medeiros, B., Sandu, I., and Ahlgrimm, M. (2015). Observed and modeled patterns of covariability between low-level cloudiness and the structure of the trade-wind layer. *J. Adv. Model. Earth Syst.*, *7*(4), 1741–1764.

Nuijens, L., Serikov, I., Hirsch, L., Lonitz, K., and Stevens, B. (2014). The distribution and variability of low-level cloud in the North Atlantic trades. *Q. J. R. Meteorol. Soc.*, *140*(684), 2364–2374. doi: 10.1002/qj.2307

Raveh-Rubin, S. (2017). Dry intrusions: Lagrangian climatology and dynamical impact on the planetary boundary layer. *J. Clim.*, *30*(17), 6661–6682. doi: 10.1175/JCLI-D-16-0782.1

Raveh-Rubin, S., and Catto, J. L. (2019). Climatology and dynamics of the link between dry intrusions and cold fronts during winter, part II: Front-centred perspective. *Clim. Dyn*, *53*(3), 1893–1909. doi: 10.1007/s00382-019-04793-2

Roca, R., Lafore, J.-P., Piriou, C., and Redelsperger, J.-L. (2005). Extratropical dry-air intrusions into the west African monsoon midtroposphere: An important factor for the convective activity over the Sahel. *J. Atmos. Sci*, *62*(2), 390–407. doi: 10.1175/JAS-3366.1

Spreitzer, E., Attinger, R., Boettcher, M., Forbes, R., Wernli, H., and Joos, H. (2019). Modification of potential vorticity near the tropopause by nonconservative processes in the ECMWF model. *J. Atmos. Sci.*, *76*(6), 1709–1726. doi: 10.1175/JAS-D-18-0295.1

Sprenger, M., and Wernli, H. (2015). The LAGRANTO Lagrangian analysis tool version 2.0. *Geosci. Model Dev*, *8*(8), 2569–2586. Retrieved from `https://gmd.copernicus.org/articles/8/2569/2015/` doi: 10.5194/gmd-8-2569-2015

Stevens, B., Bony, S., Brogniez, H., et al. (2020). Sugar, gravel, fish and flowers: Mesoscale cloud patterns in the trade winds. *Q. J. R. Meteorol. Soc.*, *146*(726), 141–152. doi: 10.1002/qj.3662

Stevens, B., Bony, S., Farrell, D., et al. (2021). EUREC $^4$A. *Earth Syst. Sci. Data Discuss.*, 1–78. doi: 10.5194/essd-2021-18

Vial, J., Bony, S., Stevens, B., and Vogel, R. (2017). Mechanisms and model diversity of trade-wind shallow cumulus cloud feedbacks: A review. In *Shallow clouds, water vapor,*

*circulation, and climate sensitivity* (pp. 159–181). Springer. doi: 10.1007/s10712-017-9418-2

Vial, J., Vogel, R., Bony, S., Stevens, B., Winker, D. M., Cai, X., et al. (2019). A new look at the daily cycle of trade wind cumuli. *J. Adv. Model. Earth Syst.*, *11*(10), 3148–3166.

Wernli, H. (1997). A Lagrangian-based analysis of extratropical cyclones: A detailed case-study. *Q. J. R. Meteorol. Soc.*, *123*(542), 1677–1706. doi: 10.1002/qj.49712354211

Yoneyama, K., and Parsons, D. B. (1999). A proposed mechanism for the intrusion of dry air into the tropical western Pacific region. *J. Atmos. Sci.*, *56*(11), 1524–1546. doi: 10.1175/1520-0469(1999)056<1524:APMFTI>2.0.CO;2

Eidgenössische Technische Hochschule Zürich
Swiss Federal Institute of Technology Zurich

# Declaration of originality

The signed declaration of originality is a component of every semester paper, Bachelor's thesis, Master's thesis and any other degree paper undertaken during the course of studies, including the respective electronic versions.

Lecturers may also require a declaration of originality for other written papers compiled for their courses.

---

I hereby confirm that I am the sole author of the written work here enclosed and that I have compiled it in my own words. Parts excepted are corrections of form and content by the supervisor.

**Title of work** (in block letters):

Diabatic processes associated with an extratropical dry intrusion reaching into the western North Atlantic trade wind region

**Authored by** (in block letters):

*For papers written by groups the names of all authors are required.*

| **Name(s):** | **First name(s):** |
|---|---|
| Müller | Sara |
| | |
| | |
| | |
| | |

With my signature I confirm that

- I have committed none of the forms of plagiarism described in the 'Citation etiquette' information sheet.
- I have documented all methods, data and processes truthfully.
- I have not manipulated any data.
- I have mentioned all persons who were significant facilitators of the work.

I am aware that the work may be screened electronically for plagiarism.

| **Place, date** | **Signature(s)** |
|---|---|
| 14.3.2021 |  |
| | |
| | |
| | |
| | |

*For papers written by groups the names of all authors are required. Their signatures collectively guarantee the entire content of the written paper.*